

The Galactic distribution of planetary nebulae with different types of dust

Diego Hernández-Juárez,^{1*} Mónica Rodríguez,² and Miriam Peña¹

¹ Universidad Nacional Autónoma de México, Instituto de Astronomía, Apdo. Postal 70264, Ciudad Universitaria, Ciudad de México, México

² Instituto Nacional de Astrofísica, Óptica y Electrónica, Luis Enrique Erro 1, Tonantzintla 72840, Puebla, México

Accepted XXX. Received YYY; in original form ZZZ

ABSTRACT

We identify different dust features in our compilation of infrared spectra for 267 planetary nebulae (PNe) from the *Spitzer*, *ISO*, and *IRAS* telescopes. We classify 206 objects according to their dust type: mixed dust (MD), oxygen-rich dust (ORD), carbon-rich dust (CRD), PNe with only polycyclic aromatic hydrocarbons (PAHs) in their spectra (oPAH), and featureless (F) PNe. We study statistically the distributions of surface brightness and diameter of PNe with different types of dust as well as their distributions in the Galaxy. We find that both MD and ORD PNe are closer to the Galactic centre than CRD and oPAH PNe, and that the Galactic distributions of each pair of groups are statistically compatible, suggesting that they have similar progenitors. Since oPAH PNe have, on average, larger diameters and lower surface brightness than CRD PNe, we suggest that oPAH PNe are evolved CRD PNe. On the other hand, F PNe have the lowest surface brightness and the largest diameters, suggesting they could contain evolved PNe from any initial type of dust. Among the PNe with silicates, we find that only a few ORD PNe have just amorphous silicates in their spectra, and their distributions of Galactocentric distances and Galactic heights suggest that they had low-mass progenitors. MD PNe with both amorphous and crystalline silicates have the largest surface brightness and the smallest diameters and might be the earliest stages of PNe with the most massive and metal-rich progenitors.

Key words: Planetary nebulae: general – dust – Galaxy: evolution – local interstellar matter

1 INTRODUCTION

Asymptotic Giant Branch (AGB) stars are one of the main sources of stellar dust in the Galaxy (see, e.g., Schneider & Maiolino 2024, and references therein). AGB stars are the descendants of stars with initial masses between 1 and 8 M_{\odot} (low- and intermediate-mass stars). During this phase, in the outermost regions of the stellar atmosphere, the suitable conditions of pressure and temperature exist for dust grains to form and grow (Whittet 2002). The critical elements that lead to dust formation are oxygen and carbon, because they are relatively more abundant than the other elements and because they can form solid compounds. Carbon and oxygen atoms combine to produce the CO molecule, a stable molecule that is difficult to dissociate, and the type of dust that an AGB forms depends on which of these two elements remains free in the stellar atmosphere. That is, the dust chemistry in the atmosphere of AGB stars is determined by the C/O abundance ratio. If $C/O > 1$ the dust chemistry will be carbon-rich, and compounds like SiC, amorphous carbon, and Polycyclic Aromatic Hydrocarbons (PAHs) are expected to form. If $C/O < 1$, the chemistry will be oxygen-rich and lead to the formation of compounds like silicates and oxides.

The C/O abundance ratio is determined by processes that occur during the AGB phase, the most important ones being the third dredge-up (TDU) and hot bottom burning (HBB, Scalo et al. 1975; Iben & Renzini 1981). The TDU leads to the mixing of carbon-rich material to the outer layers of the star, whereas HBB destroys car-

bon and produces nitrogen at the base of the star’s convective envelope. Stellar evolution models differ on the precise mass limits at which these processes occur and in their efficiency (Weiss & Ferguson 2009; Karakas & Lugaro 2016; Ventura et al. 2018; Rees et al. 2024). In general, the models predict that the range of progenitor masses leading to carbon-rich objects is very wide at low metallicities and gets progressively narrower as the metallicity increases. At solar metallicity, the envelopes of AGB stars with initial masses of $\sim 2\text{--}4 M_{\odot}$ will end up being carbon rich, whereas stars outside this range of masses, with lower and higher initial masses, will remain oxygen rich. At low metallicities, most AGB stars will have carbon-rich envelopes and, at metallicities above solar, most objects will end up being oxygen rich.

After the AGB phase, the star evolves to the planetary nebula (PN) phase, where the dust is preserved (Stasińska & Szczerba 1999). The analyses of the dust composition in PNe of the Magellanic Clouds (Stanghellini et al. 2007) and Galactic PNe (Stanghellini et al. 2012) have shown that the predictions of stellar evolution models are in broad agreement with the observations. Stanghellini et al. (2007, 2012) use infrared spectra from the *Spitzer Space Telescope* to classify 66 PNe of the Magellanic Clouds and 150 Galactic PNe into featureless objects (with black-body emission but no dust features), objects with carbon-rich dust, objects with oxygen-rich dust, and mixed-dust objects (with emission features attributed to silicates and PAHs). They find that at the low metallicities of the Magellanic Clouds, most of the PNe are featureless or carbon rich, with just 7 per cent of oxygen-rich PNe and no mixed-dust objects, whereas the higher metallicity of the Galaxy leads to the formation of many

* E-mail: dbhernandez@astro.unam.mx

oxygen-rich and mixed-dust PNe, with the latter mainly located near the Galactic centre.

García-Hernández & Górný (2014) study the physical conditions and chemical abundances and dust types of their sample of 131 Galactic PNe, and compare their results with the predictions of stellar evolution models. They conclude that mixed-dust PNe are the dominant population in the Galactic bulge and have high metallicity, massive progenitors, with masses between 3 and 5 M_{\odot} . On the other hand, they find that PNe with oxygen-rich and carbon-rich dust are mostly in the Galactic disc and have low metallicity progenitors with lower masses (1–1.5 M_{\odot} for the oxygen-rich PNe, 1.9–3 M_{\odot} for the carbon-rich PNe), although they mention that a few oxygen-rich PNe and a significant fraction of carbon-rich objects could have more massive progenitors. García-Hernández & Górný (2014) also argue that featureless PNe are evolved PNe that had both high and low metallicity progenitors.

Delgado-Inglada et al. (2015) explore further the relation between chemical abundances and dust types in Galactic PNe by restricting the analysis to 20 objects that have good-quality optical spectra. They confirm that PNe with carbon-rich dust mostly have intermediate masses and low metallicities and that PNe with mixed dust had progenitors with the highest masses and metallicities. However, they find that most of their sample PNe with oxygen-rich dust also had high-mass, high-metallicity progenitors, although this difference with the results of García-Hernández & Górný (2014) could be due to the fact that the sample of Delgado-Inglada et al. (2015) is small.

Some of these results are based on small samples, or depend on uncertain distance estimates, or use optical spectra of poor quality. Besides, there are stellar and nebular parameters that could be related to the mass and metallicity of the PN progenitor stars, and whose relationship with the type of dust found in the nebula has not been explored. In this paper, we present a compilation of infrared spectra for 266 PNe from the *Spitzer*, *ISO*, and *IRAS* telescopes (§2). With these spectra we classify 205 PNe according to their type of dust (§3), obtaining a sample that is 40 per cent larger than previous ones. We compare our classification to previous ones, finding differences in some cases (§4). We then search for relations between the PN dust type and the nebular diameter, $H\alpha$ surface brightness, and Galactic distribution (§5 and §6). Our conclusions are presented in §7. The relations between the type of dust and other parameters, such as the nebular morphology and the spectral type of the central star, will be explored in a future paper.

2 COMPILATION OF INFRARED SPECTRA

Most of our sample was compiled from the *Spitzer Space Telescope* database. We used the NASA/IPAC Infrared Science Archive,¹ where we looked for those programs centred in Galactic PNe or that contained observations for objects classified as ‘true PNe’ in the HASH database (Hong Kong/AAO/Strasbourg $H\alpha$ Planetary Nebulae Database, Parker et al. 2016). The programs we use are the following: 45 (Principal Investigator, PI: Roelling, 11 PNe), 77 (PI: Rieke, 4 PNe), 93 (PI: Cruikshank, 4 PNe), 3235 (PI: Waelkens, 2 PNe), 3633 (PI: Bobrowsky, 40 PNe), 20049 (PI: Kwitter, 1 PNe), 20590 (PI: Sahai, 2 PNe), 30430 (PI: Dinerstein, 6 PNe), 30550 (PI: Houck, 8), 30652 (PI: Bernard-Salas, 2 PNe), 40115 (PI: Fazio, 3 PNe), 40035 (PI: Bernard-Salas, 3 PNe), 50168 (PI: De Marco, 5 PNe), and 50261 (PI: Stanghellini, 131 PNe).

¹ <https://irsa.ipac.caltech.edu/applications/Spitzer/SHA/>

The spectrometer in the *Spitzer Space Telescope*, the Infrared Spectrograph (IRS), has four modules covering the wavelength range 5.2–38.0 μm (Werner et al. 2004; Houck et al. 2004). Two modules have a variable low-resolution, between 6 and 128, and cover the full wavelength range, whereas the other two modules have a resolution of 600 in the range from 9.9 to 37.2 μm .

We used the spectra taken with the four spectrograph modules of *Spitzer*, removing bad pixels and rescaling parts of the spectra when necessary. We also added the two spectra available for each object in the *Spitzer* database. These corrections were made with the SMART program (Higdon et al. 2004). The spectra of the low resolution modules have available a sky-subtracted version. In order to avoid background contamination, we use these sky-subtracted spectra to look for the PAH features, although background contamination is not expected to be important in most cases (Stanghellini et al. 2012). When the higher resolution spectra are available, we use them to look for the other dust features. We show in Appendix A the *Spitzer* spectra that, as far as we know, have not been previously published.

To obtain the largest possible sample, we also searched for published spectra from the *ISO* Short Wave Spectrometer (SWS) (Kessler 2002) and *IRAS* Low Resolution Spectrometer (LRS) (Helou 1995). *ISO/SWS* covered the 2.4–45 μm band with spectral resolutions in the range 1000–35000. *IRAS/LRS* covered the 7.7 to 22.7 μm wavelength range with a spectral resolution of 20–60. We only looked for *ISO* and *IRAS* spectra for objects that have no *Spitzer* spectra, and we only used works that show the observed spectra in figures where we can identify or confirm the presence or absence of the dust features.

In total, we have compiled spectra for 267 PNe: 220 from *Spitzer*, 12 from *ISO*, 27 from *IRAS*, 5 with spectra from *IRAS* and *ISO*, and 3 that have different parts of the spectra observed by *Spitzer* and *ISO*. The spectra from *IRAS* have the most limited wavelength coverage, 7.7–22.7 μm (Emerson et al. 1985). Besides, for those objects with *Spitzer* spectra, 7 do not have data between 5.2 and 19.9 μm , and 10 objects only have data for this wavelength range.

More than 50 per cent of our sample comes from the *Spitzer* program 50261, which searched for compact PNe (with angular diameters below 4’). For this reason, a large part of our sample is likely to be composed of young PNe, although some compact PNe can be old and distant (Stanghellini et al. 2012). Besides, a significant part of our sample comes from works centred in the study of PNe with mixed-chemistry dust (as the objects from Perea-Calderón et al. 2009). These sample characteristics may introduce biases that should be considered when analysing the results.

3 DUST FEATURES AND PNE CLASSIFICATION

In all the compiled infrared spectra from *Spitzer*, *ISO*, and *IRAS*, we search for features of PAHs, silicon carbide (SiC), amorphous and crystalline silicates, and a broad feature around 30 μm . These are the most easily identified features in the infrared spectrum region we are analysing and have been frequently studied.

In the wavelength range that we are considering, features that are usually attributed to PAHs can be detected at 6.2, 7.7, 8.6, 11.2, 12.3, and 12.6 μm (Allamandola et al. 1989). Most of these features can be clearly seen in the spectrum of the PN Hen 2-86, which we show in Fig. 1 for illustrative purposes. The approximate positions of these PAH features are marked with pink stripes in the figure.

The most prominent feature due to amorphous silicates is detected at $\sim 10 \mu\text{m}$. There is another feature due to amorphous silicates at $\sim 18 \mu\text{m}$, but we do not use it for classification purposes because two

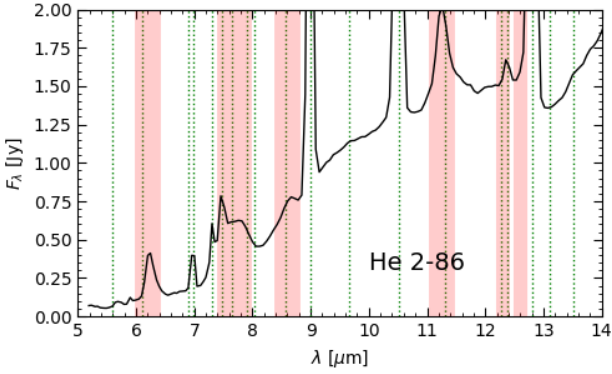


Figure 1. Example of a spectrum with PAH features, whose expected positions are indicated with pink stripes. The green dotted lines show the wavelengths of nebular emission lines: Mg v] 5.60 μm , H₂ S(6) 6.10 μm , H₂ S(5) 6.90 μm , He I 6.99 μm , [Na III] 7.31 μm , H I 7.48 μm , [Ne IV] 7.65 μm , [Ar V] 7.90 μm , H₂ S(4) 8.03 μm , [Ne IV] 8.56 μm , H₂ S(3) 9.66 μm , [S IV] at 10.51 μm , H I 11.30 μm , H₂ S(2) 12.28 μm , He I 12.39 μm , [Ne II] 12.82 μm , [Ar V] 13.10 μm , and [Mg V] 13.52 μm .

parts of the *Spitzer* spectrum are spliced together in this region. The features of crystalline silicates are located at around 23, 28, and 33 μm . All these silicate features are illustrated for the PN IC 4776 in Fig. 2 (top panel).

The SiC feature can be seen at around 11 μm , and there is another feature associated with carbon-rich environments at 30 μm . Some suggestions of compounds that could explain the 30 μm feature are magnesium sulfide (MgS, Goebel & Moseley 1985; Nuth et al. 1985), hydrogenated amorphous carbon (Grishko et al. 2001), and molecules similar to PAHs (Papoular 2011). The features of SiC and 30 μm are shown for the PN Hen 2-26 in the middle panel of Fig. 2.

Some PNe do not have any clear dust features in their spectrum, although they do show blackbody-like emission, most probably due to dust emission. The bottom panel of Fig. 2 shows an example of this kind of featureless spectra.

The sample PNe are classified into five groups depending on the dust features present in their spectra: (i) oxygen-rich dust (ORD) PNe, with amorphous silicates and/or crystalline silicates; (ii) mixed-dust (MD) PNe, with PAHs plus amorphous silicates and/or crystalline silicates; (iii) carbon-rich dust (CRD) PNe, with SiC and/or the 30 μm feature, with or without PAHs; (iv) only PAH (oPAH) PNe, with PAHs and no other dust features; and (v) featureless (F) PNe, with no dust features. These groups are similar to those defined by other works, with the exception of the oPAH group, which was included in the CRD group in previous analyses (Stanghellini et al. 2012; García-Hernández & Górný 2014). We define here the oPAH PNe as a separate group because PAHs are found both in CRD and MD PNe (Górný et al. 2001; Guzmán-Ramírez et al. 2012).

From our original sample of 267 PNe with available infrared spectra, 216 have a full spectrum in the range from 5 to 38 μm and most of them, 202 PNe, can be classified into the dust groups defined above, whereas the remaining 13 PNe have low signal-to-noise spectra that prevents their classification, although their spectra can be used to verify the presence or absence of some dust features. On the other hand, four objects that have incomplete spectra, DdDm 1, Hb 5, Hu 2-1, and NGC 6826, can be classified as CRD PNe because they have the SiC feature or the 30 μm feature. Therefore, the sample that can be classified following the procedure described above contains 206 PNe with a well-defined type of dust. Table 1 shows the numbers and percent-

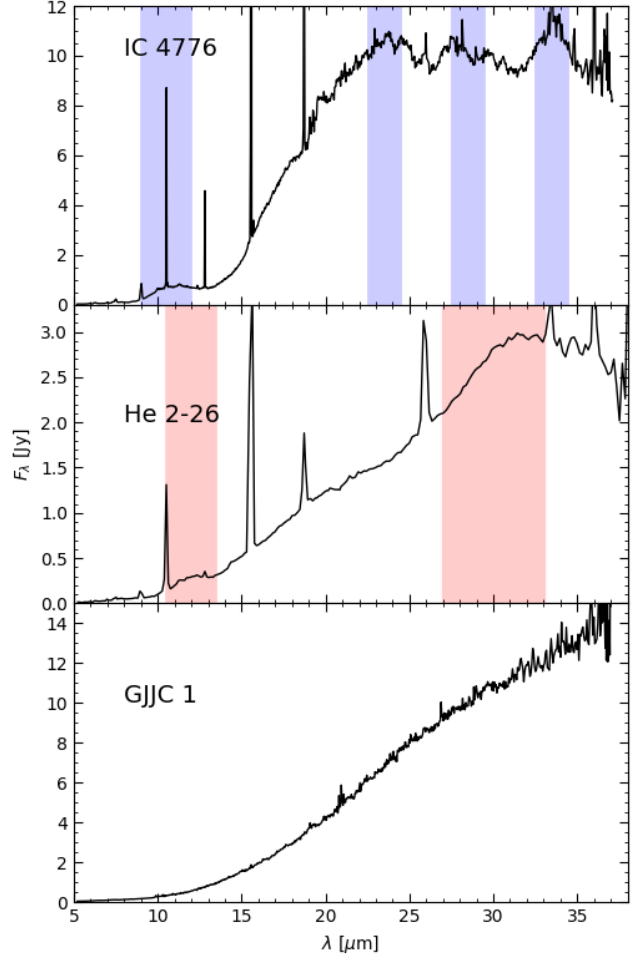


Figure 2. Top panel: spectrum of IC 4776, which shows features of amorphous silicates at ~ 10 μm and crystalline silicates at ~ 23 , 28 and 33 μm , as indicated with the blue stripes. Middle panel: spectrum of Hen 2-26 showing the SiC feature at around 11 μm and the 30 μm feature, both marked with pink stripes. Bottom panel: spectrum of GJJC 1, a PN with no apparent dust features.

ages of PNe in each group and subgroup. This sample is ~ 40 per cent larger than the largest sample previously analysed (Stanghellini et al. 2012, with 150 PNe).

Of the initial sample of 267 PNe, 61 objects could not be classified because they had incomplete or noisy spectral information, but we have compiled some information on the presence or absence of dust features in their spectra. Thus, information for a total of 267 PNe has been gathered. The number of PNe that have the different features is given in Table 2, where the first column indicates the feature; the second column gives the number of PNe where the spectral range in which we can see the features is available; and the third column lists the number of PNe that show the feature and the percentage of PNe with the feature. The most common features are those attributed to PAHs and silicates, while the SiC and 30 μm features are less frequent. Among the silicates, most of them are crystalline.

The features identified for each object and the types of dust assigned to them are presented in Table B1 in Appendix B, along with the references for their published spectra.

Table 1. Numbers of PNe with different types of dust. The percentages in the second column are for the full sample, whereas the percentages in the last column are for each type of dust.

Type	N (%)	Features	N (%)
MD	72 (35 %)	Crystalline silicates, PAHs	50 (70 %)
		Am. and crys. silicates, PAHs	22 (30 %)
ORD	52 (25 %)	Amorphous silicates	13 (25 %)
		Crystalline silicates	24 (46 %)
		Am. and crys. silicates	15 (29 %)
CRD ^a	35 (17 %)	SiC, can have PAHs	10 (29 %)
		30 μm , can have PAHs	7 (20 %)
		SiC and 30 μm , can have PAHs	18 (51 %)
oPAH	12 (6 %)	PAHs	
F	35 (17 %)	No features	
Total	206 (100 %)		

^a There are 17 CRD PNe with PAH features (49 %): 3 of them show the SiC feature, 2 show the 30 μm feature, and 12 have both SiC and the 30 μm feature in their spectra.

Table 2. PNe with specific dust features. In the percentage indicated in the last column, we only consider those PNe with data in the spectral range where we can see the feature.

Feature	PNe with data	PNe with the feature
SiC	224	28 (12 %)
30 μm	230	25 (11 %)
PAHs	224	100 (45 %)
Amorphous silicates	224	50 (22 %)
Crystalline silicates	230	113 (49 %)

4 COMPARISON WITH PREVIOUS CLASSIFICATIONS

The largest samples of PNe classified into different dust types are those presented by Stanghellini et al. (2012) and García-Hernández & Górný (2014). Stanghellini et al. (2012) present *Spitzer* spectra for 157 PNe² and classify 150 of them into four groups, three of them similar to those of this work (MD, ORD, and F) and one that includes the objects that we classify as CRD and oPAH PNe here. García-Hernández & Górný (2014) include 148 PNe in their classification, and follow a classification scheme similar to that of Stanghellini et al. (2012).

Our classification contains 206 objects, including the PNe studied by Stanghellini et al. (2012) and García-Hernández & Górný (2014), and there are differences in the classification of some objects. We have 14 PNe with a different dust type than the one assigned by Stanghellini et al. (2012) and 16 PNe with a different type than the one assigned by García-Hernández & Górný (2014). An example of this is Al2-E (PN G359.3+03.6), in whose spectrum we do not observe crystalline silicate features, but Stanghellini et al. (2012) and García-Hernández & Górný (2014) do. We list the objects with different classification in Table C1 in Appendix C. The number of objects with a different classification is small, and our results in the following sections are not affected by these objects.

In the case of the *ISO* and *IRAS* spectra, all of which have already been published by other authors, some of these authors also identify the dust features, and these identifications agree with ours.

5 NEBULAR DIAMETER AND SURFACE BRIGHTNESS

García-Hernández & Górný (2014) argue that F PNe are more evolved than other types of PNe since they have lower electron densities and higher degrees of ionization. Here we explore the evolutionary status of PNe with different types of dust using their surface brightness and nebular diameters, since these parameters can also be expected to change during the lifetime of a PN.

We use the values of intrinsic $H\alpha$ surface brightness calculated by Frew et al. (2016), which are available for 63 per cent of our sample with a well-defined dust type. As for the diameters, we calculate their values using the angular diameters listed in the HASH database (Parker et al. 2016) and the most reliable distances from Hernández-Juárez et al. (2024). These distances are based on more than one distance estimate (cases A, B, and C in Hernández-Juárez et al. 2024). We can calculate the diameter for 71 per cent of our sample with a well-defined dust type.

The left panels of Fig. 3 show the distributions of both parameters, $H\alpha$ surface brightness and nebular diameter, for PNe with different types of dust, with the numbers in parentheses indicating the sample sizes. The medians of the distributions are indicated with the dashed lines. We can see in Fig. 3 that the oPAH and, even more so, the F PNe, have lower brightness and larger diameters in average than the MD, CRD, and ORD PNe.

The statistical significance of the similarities and differences between the distributions shown in Fig. 3 can be studied with Kolmogorov-Smirnov tests (K-S, Press & Saul 2007). The results from these tests are the p -values, the probabilities that the differences in the cumulative distributions of two samples can be explained by statistical fluctuations if the two samples had the same original distribution. The p -values of the one-dimensional K-S tests that compare each possible pair of distributions are listed in the right panels of Fig. 3. A large p -value indicates that the two distributions are compatible (they might have the same original distribution or the differences are too small to be detected with the available data); a small p -value indicates that there are significant differences between the samples.

The one-dimensional K-S tests that we are using require that the effective number of data for the two distributions to be compared, $N_e = N_1 N_2 / (N_1 + N_2)$, is larger or equal to 4, with N_1 and N_2 the sizes of the two distributions. This condition holds for all the one-dimensional K-S tests presented in this work. The lowest values of N_e are found for the comparisons between oPAH and CRD PNe, with $N_e = 5-9$.

As we can see from the p -values in Fig. 3, MD, ORD, and CRD PNe have similar distributions of surface brightness and diameters, oPAH PNe have significantly lower surface brightness and larger diameters than these types, and F PNe have on average the lowest surface brightness and largest diameters of all dust types. This suggests that PNe lose their infrared dust features as they evolve and that oPAH could be evolved nebulae that were originally MD or CRD PNe whereas F PNe are even more evolved nebulae that were originally MD, ORD, CRD, or oPAH PNe. The connections between these types of dust are further explored in the next section, although we should also keep in mind that oPAH and F PNe might contain objects that had different progenitors from those of the other dust types (less massive, or with lower metallicity, or with $C/O \sim 1$).

² a

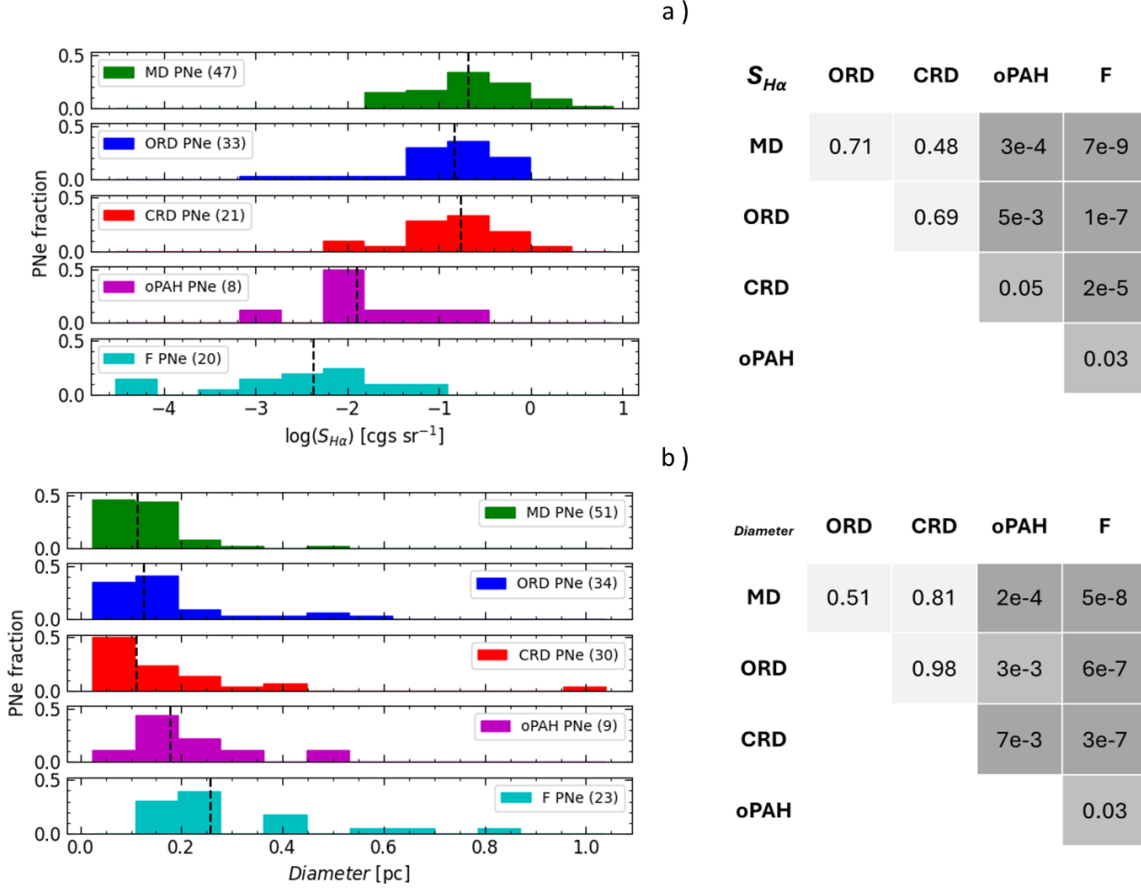


Figure 3. Distributions (left panels) and p -values (right panels) of: a) the $H\alpha$ surface brightness of PNe, and b) the PN diameters, for different types of dust. The dashed lines in the left panels indicate the medians of the distributions. The right panels show the results of Kolmogorov-Smirnov (K-S) tests between each pair of dust types, with the lightest cells indicating similar distributions, and the darkest cells indicating significantly different distributions.

6 GALACTIC DISTRIBUTION

Fig. 4 shows the distributions in the sky, in Galactic coordinates, of PNe with different types of dust. Most MD and ORD PNe can be seen to be located preferentially towards the Galactic center, whereas CRD and oPAH PNe have wider distributions in Galactic longitude. This is consistent with the Galactic distribution of oxygen-rich and carbon-rich AGB stars (see Lewis et al. 2020, and references therein) if we assume that the progenitors of MD and ORD PNe were oxygen-rich AGB stars whereas the progenitors of CRD and oPAH PNe were carbon-rich AGB stars.

On the other hand, the distributions of Galactic latitudes in Fig. 4 drop at latitudes close to zero, especially for MD, ORD, and F PNe. Since these are also the PNe that are located mostly in the direction to the Galactic centre, this result indicates that we are missing many MD, ORD, and F PNe which are located close to the Galactic plane.

6.1 Heliocentric distances

In order to explore the Galactic distribution of our sample PNe, we need their distances. We have good distance estimates for 182 PNe of the sample of 205 PNe with a well-defined type of dust. This is nearly double the sample of 92 Galactic PNe used by Stanghellini et al. (2012) to study the Galactic distribution of PNe with different types of dust. As in §5, the distances we use are the most reliable ones of those calculated by Hernández-Juárez et al. (2024). One of

the sample PNe, BoBn 1 (PN G108.4–76.1, an oPAH PN), belongs to the Galactic halo (Quireza et al. 2007), and we have excluded it from the analyses that follow. Therefore, we can study the Galactic distribution of 88 per cent of our sample with a well-defined type of dust.

Since the distance uncertainties are larger for the most distant sources, if the different types of dust have different distributions of heliocentric distances, this can introduce biases in our results. Hence, we first examine the heliocentric distance distribution of each type of PNe. The left panel of Fig. 5a shows these distributions, whereas the right panel shows the p -values obtained by comparing each pair of distributions with one-dimensional K-S tests. The p -values are all larger than 0.14, implying that there are no significant differences in the distributions of heliocentric distances of PNe with different types of dust.

6.2 Galactic distribution of PNe with different types of dust

The middle and bottom left panels of Fig. 5 show the distributions of Galactocentric distances, R_G , and the projections on the Galactic plane of PNe with different types of dust. The plane of the Galaxy is shown as seen from positive Galactic height and centred on the Sun. The position of the Galactic center (GC in the figure) is also indicated, and the distance uncertainties are shown with lines.

The middle and bottom right panels of Fig. 5 show the p -values

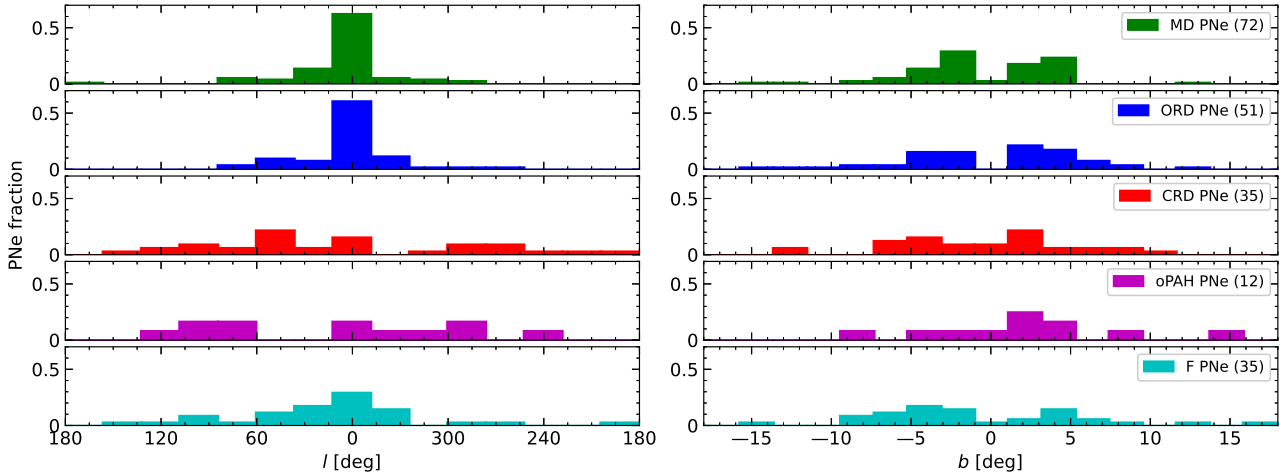


Figure 4. Distributions of Galactic longitude (l) and latitude (b) of PNe with different types of dust. The numbers in the parentheses indicate the sample sizes. Five PNe lie outside the range plotted for b : MaC 2-1 (PN G205.8–26.7, CRD), NGC 6210 (PN G043.1+37.7, ORD), BoBn 1 (PN G108.4–76.1, oPAH), NGC 246 (PN G118.8–74.7, F), and NGC 7094 (PN G066.7–28.2, F).

that result when we compare each pair of distributions using K-S tests (Fasano & Franceschini 1987; Press & Saul 2007). The K-S tests confirm that the similarities and differences that can be seen in the middle and bottom left panels of Fig. 5 are statistically significant. As previously mentioned, the one-dimensional K-S tests are valid when the effective number of data for the two distributions to be compared, N_e , is larger or equal to 4. On the other hand, the two-dimensional K-S tests used to compare the distributions of PNe in the Galactic plane require $N_e \geq 20$ and this condition is valid only for the comparisons between the MD PNe and the ORD, CRD, and F PNe (the p -values that are based on an insufficient number of data are enclosed in parentheses in the bottom right panel of Fig. 5). However, the p -values derived from the two-dimensional K-S tests that compare the distributions on the Galactic plane are mostly in agreement with those derived from the one-dimensional K-S tests that compare the distributions of Galactocentric distances. We only show them for comparison purposes, and the conclusions presented below are based on the p -values implied by the one-dimensional K-S tests, all of which are statistically valid.

The results presented in Fig. 5 indicate that MD and ORD PNe are more abundant towards the Galactic center than CRD, oPAH, and F PNe. Previous works also find that many MD PNe are close to the Galactic centre, but conclude that ORD PNe have distributions intermediate between those of MD and CRD objects (Stanghellini et al. 2012; García-Hernández & Górný 2014). The differences among the results might be due to the procedure followed by García-Hernández & Górný (2014) to assign PNe to different parts of the Galaxy or to the use of Stanghellini et al. (2012) of a smaller sample with no statistical comparisons between the distributions. Indeed, the p -values shown in Fig. 5 indicate that MD and ORD PNe are distributed in a very similar way in the Galaxy.

It can also be seen in Fig. 5 that oPAH and CRD PNe also have very similar distributions. So, each pair of groups seems to have a common origin. Besides, the distributions of MD and ORD PNe are significantly different from those of oPAH and CRD PNe, whereas F PNe have intermediate distributions that in most cases are significantly different from the other dust types. Taking into account the results found in §5, we conclude that most oPAH PNe are likely to be evolved CRD PNe, whereas F PNe can be even more evolved PNe that originally belonged to any of the other dust types. The groups

oPAH and F can also contain or be composed of objects where a low metallicity, or a C/O abundance ratio close to one, prevented the formation of the dust compounds that we are studying. However, at least in the case of oPAH PNe, their initial masses and metallicities should not be very different from those of CRD PNe, because the distributions in the Galaxy of the two groups are very similar.

Evolved PNe might lose their emission in a dust feature if the dust grains become too cold to emit, or if they are altered or destroyed. For example, some compounds, such as fullerenes or graphite, might form on the surface of SiC grains and prevent us from observing the SiC feature (Bernal et al. 2019).

The similarities between the distributions of MD and ORD PNe suggests that MD PNe were originally ORD objects and some process led to the formation of PAHs in their vicinity. There are several scenarios that can explain the formation of PAHs in an environment that contains silicates (see, e.g., Perea-Calderón et al. 2009; Guzman-Ramirez et al. 2011, and references therein), such as a very late thermal pulse that turns an oxygen-rich outflow into a carbon-rich one (Waters et al. 1998), or the dissociation of CO in a dense torus irradiated by the central star (Matsuura et al. 2004; Cernicharo 2004; Guzman-Ramirez et al. 2011; Cox et al. 2016).

The increase of MD and ORD PNe towards the Galactic centre suggest that these objects arise more easily from progenitors with higher metallicity, as predicted by most models of stellar evolution (see, e.g., Karakas 2014). Previous results based on nitrogen and helium abundances suggest that the highest progenitor masses should be found among MD PNe, followed by ORD PNe (García-Hernández & Górný 2014; Delgado-Inglada et al. 2015). Besides, although some ORD PNe have been found in the Magellanic Clouds, no MD PNe have been found in these low-metallicity galaxies. Hence, we suggest that only the most massive and metal-rich oxygen-rich progenitors can form MD PNe. Perea-Calderón et al. (2009) argue that dual-dust chemistry is related to low-mass progenitors, but this conclusion seems to be based on the assumption that that all bulge PNe, where this phenomenon is prevalent, had old low-mass progenitors. Since there is a significant population of young stars in the Galactic bulge (see Hasselquist et al. 2020, and references therein), this might not be the case.

We do not explore the distributions of distances to the Galactic plane for the different types of dust because our sample is not big

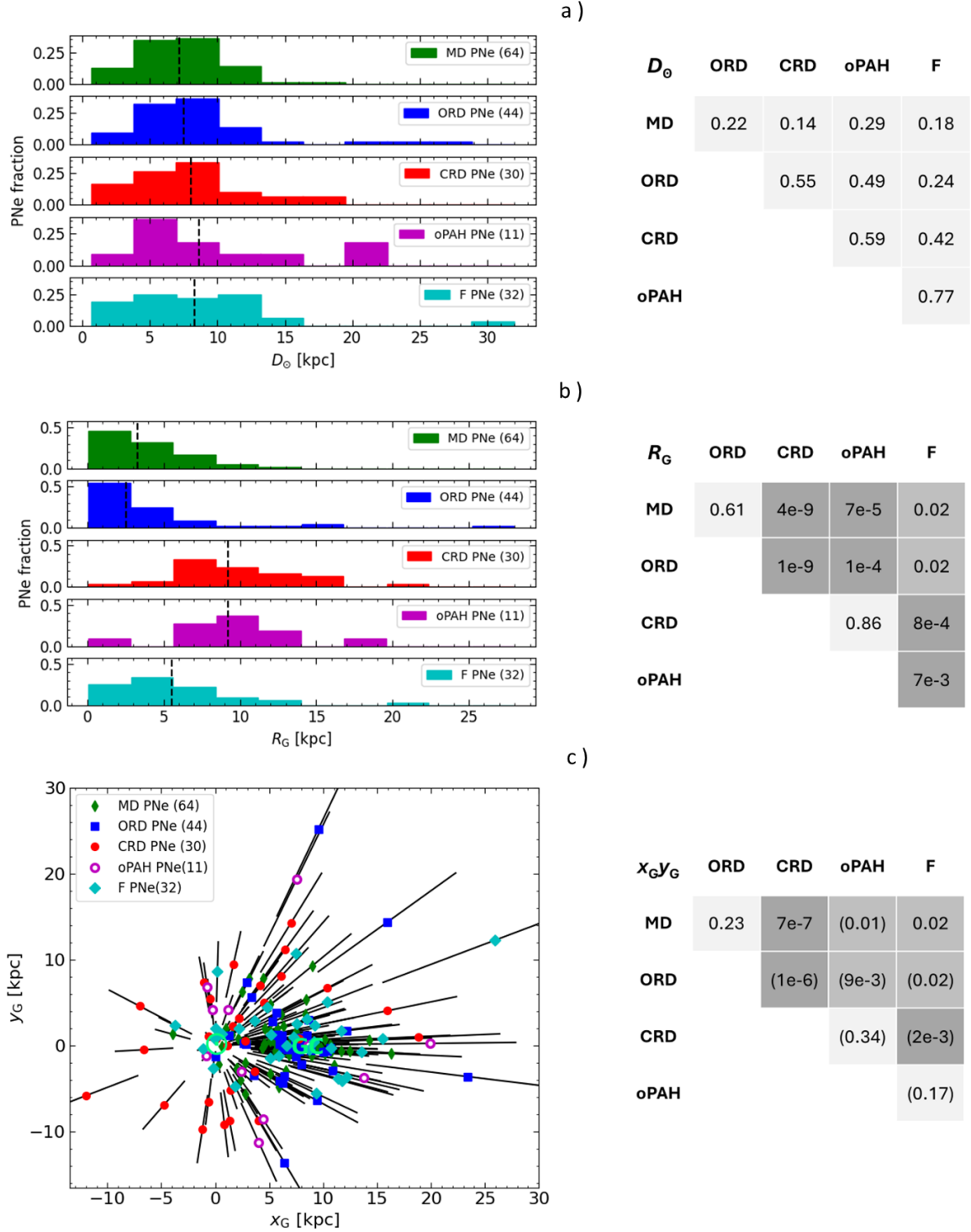


Figure 5. Distributions (right panels) and p -values (left panels) of a) heliocentric distances; b) Galactocentric distances; and c) projection on the Galactic plane of PNe with different types of dust. The dashed lines in the top and middle left panels indicate the medians of the distributions. In the bottom left panel, the positions of the Sun (0, 0) and the Galactic centre (8, 0) are marked in green as “ \odot ” and “GC”, and the lines show the distance uncertainties. The right panels show the p -values obtained from one dimensional K-S tests that compare each pair of distributions. The darkest cells in these panels indicate significant differences between the distributions. The p -values that are based on an insufficient number of data are enclosed in parentheses

enough in the solar neighbourhood (see Fig. 5), because the different types of dust have different Galactic distributions, and because we are missing many oxygen-rich PNe located close to the Galactic plane in the direction of the Galactic centre (see Fig. 4).

6.3 Galactic distribution of different dust features

We have explored the Galactic distributions and the distributions in surface brightness and diameters of the different dust features that we identify in the spectra. In most cases, these distributions reflect the distributions of the PN dust types that contain the feature, and do not provide new insights into the origins of the PN hosting the feature. The exceptions are the distributions of amorphous and crystalline silicates in MD and ORD PNe, and below we discuss only the results concerning these features that have any statistical significance (with p -values of a few per cent or lower).

We divide the sample MD and ORD objects into PNe with only crystalline silicates, PNe with both crystalline and amorphous silicates, and PNe with only amorphous silicates.

Stanghellini et al. (2012) mention that ORD PNe with crystalline silicates have typically lower Galactic latitudes than ORD PNe with amorphous silicates. From this, they suggest that the progenitor stars of crystalline ORD PNe had higher masses than the progenitors of amorphous ORD PNe. Here, we revise this results using the Galactic distributions of our sample objects. We find that, of the 205 PNe classified into dust types, 13 objects show only amorphous silicates in their spectra, and all of them are ORD PNe. On average, these objects have higher Galactocentric distances and reach higher distances from the Galactic plane than the other ORD (or MD) PNe. The differences are significant with a confidence level of 92–96 per cent (i.e. p -values of 0.04–0.08). In agreement with Stanghellini et al. (2012), we conclude that PNe with only amorphous silicates are ORD objects that probably had progenitors with lower masses and metallicities than PNe that also show crystalline silicates in their spectra.

The higher metallicity near the Galactic centre can lead to higher mass-loss rates and a more efficient crystallization of silicates (Waters et al. 1996; Molster et al. 1999; García-Hernández & Górný 2014). The crystallization of silicates can occur before the PN phase (Cami et al. 1998; Sylvester et al. 1999; Kemper et al. 2001; de Vries et al. 2014), but if the process continues in the PN stage, we might find that PNe with crystalline silicates are on average more evolved than PNe with amorphous silicates. The possible relationship between crystalline silicates and PNe evolution has been explored by García-Hernández & Górný (2014), with mixed results. We explore here the distributions of $H\alpha$ surface brightness and physical diameter for MD and ORD PNe that show different types of silicate features in their spectra. The distributions for the 9–10 PNe with only amorphous silicates that have information on the surface brightness and diameter do not show any significant difference from those of PNe with only crystalline silicates or with both types of silicate, and are not discussed further. The distributions of $H\alpha$ surface brightness and physical diameter for MD and ORD PNe with only crystalline silicates and with both crystalline and amorphous silicates are shown in Fig. 6.

We can see by comparing the medians of the distributions in Fig. 6 that ORD PNe have slightly lower surface brightness and slightly larger diameters than MD PNe. As shown in §5, the differences, although consistent with each other, are not statistically significant when the whole sample of MD and ORD PNe are considered. However, there are significant differences between MD and ORD PNe for those objects that show both types of silicates in their spectra, with p -values of 0.003 for the comparison of surface brightness and 0.02

for the comparison of diameters. Besides, MD PNe with only crystalline silicates have significantly lower surface brightness and larger diameters than MD PNe with both types of silicates, with p -values of 0.0001 for the two comparisons. In fact, MD PNe with both crystalline and amorphous silicates are clearly distributed towards larger surface brightness and smaller diameters than all other MD and ORD PNe. On the other hand, ORD PNe with only crystalline silicates have somewhat lower surface brightness and larger diameters than ORD PNe with both crystalline and amorphous silicates, although in this case the differences are smaller and are not statistically significant, with p -values of 0.1 and 0.3 respectively.

In addition to these differences in surface brightness and diameter, we know that no MD and only a few ORD PNe have been found in the low-metallicity environments of the Magellanic Clouds³ (Stanghellini et al. 2007), that MD and ORD PNe in our Galaxy are much more abundant near the Galactic centre, and that the highest metallicities and the highest abundances of nitrogen and helium are found in ORD and, especially, in MD PNe (García-Hernández & Górný 2014; Delgado-Inglada et al. 2015). Hence, our interpretation of the results presented in Fig. 6 is that most ORD and MD PNe had high-metallicity progenitors, the most massive of which led to the formation of MD PNe. The high metallicity and/or mass of these MD PN progenitors leads to conditions where silicates can easily crystallize. The high-metallicity ORD and MD PNe initially contain both amorphous and crystalline silicates, but can evolve to form ORD and MD PNe that contain only crystalline silicates. Finally, newly-formed MD PNe have both amorphous and crystalline silicates, high surface brightness and small diameters.

7 CONCLUSIONS

In this work, we have compiled the infrared spectrum of 267 PNe from the *Spitzer*, *ISO*, and *IRAS* space telescopes. We have used these spectra to identify different dust features: PAHs, SiC, amorphous and crystalline silicates, and a broad feature around 30 μm . With these identifications, we can classify 206 of the sample PNe into five groups: MD (PNe with PAHs and silicates), ORD (PNe with silicates), CRD (PNe with SiC and/or the 30 μm feature, some of them with PAHs), oPAH (PNe with only PAHs) and F (featureless PNe).

Most of the objects in our sample are MD PNe (35 per cent), followed by ORD PNe (25 per cent), CRD and F PNe (17 per cent each), and oPAH PNe (6 per cent). Our sample is almost 40 per cent larger than samples analysed in previous works, and we compare the distributions of surface brightness and diameters of the different dust types as well as their distribution in the Galaxy using K-S tests to assess the significance of the similitudes and differences.

The distributions of nebular diameters and $H\alpha$ surface brightness indicate that oPAH and F PNe are significantly more evolved than the other groups, with F PNe being the most evolved objects, i.e., the ones with the lowest values of surface brightness and the largest diameters. Since oPAH and CRD PNe have similar distributions in the Galaxy, this suggests that oPAH PNe are evolved CRD PNe. On the other hand, and considering also the distribution in the Galaxy of the different dust types, F PNe could be evolved PNe from any initial dust type (though probably mainly evolved MD and ORD PNe). PNe with low-mass and low-metallicity progenitors, and PNe with limited

³ Jones et al. (2017) found more ORD PNe than CRD PNe in the Large Magellanic Cloud. However, since their classification criteria is based on the presence or absence of PAH features, their ORD group includes all F PNe, which are the dominant population in this galaxy (Stanghellini et al. 2007).

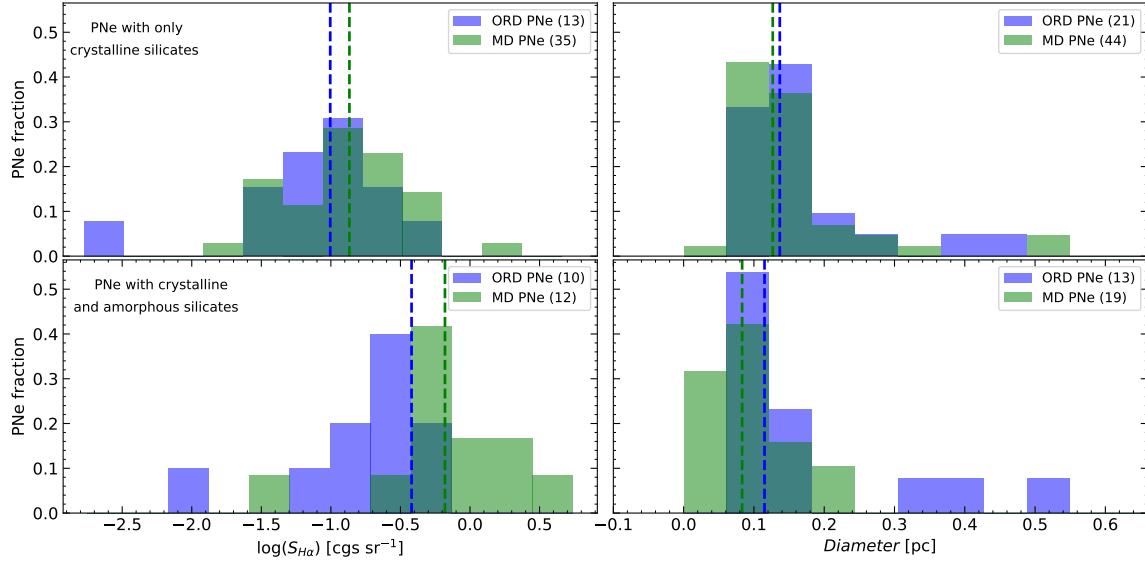


Figure 6. Distributions of $H\alpha$ surface brightness and physical diameter for MD and ORD PNe with only crystalline silicates (top panels) and with both crystalline and amorphous silicates (bottom panels). The dashed lines indicate the medians of the distributions.

dust formation because of a C/O ratio close to 1 in their ejecta, might also be F PNe, although we note that all F PNe show blackbody-like emission in their spectra.

MD and ORD PNe are heavily concentrated towards the Galactic centre, and their distributions in the Galaxy are statistically very similar. CRD and oPAH PNe are more evenly distributed across the Galactic disc, and their distributions are also statistically similar to each other. We conclude that each pair of groups had very similar progenitors. We can also conclude that the formation of ORD and MD PNe is favoured by the higher metallicities near the Galactic centre, whereas lower metallicities favour the formation of CRD and oPAH PNe, in agreement with the predictions of models of stellar evolution, like those by Karakas (2014).

We have also compared the distributions of MD and ORD PNe that have (i) only crystalline silicates in their spectra, (ii) both crystalline and amorphous silicates, and (iii) only amorphous silicates. There are no MD PNe with only amorphous silicates in their spectra, and the few ORD PNe with only amorphous silicates tend to be, on average, farther away from the Galactic centre and from the Galactic plane than the other MD and ORD PNe. This suggests that their progenitors were low-mass, low-metallicity objects. MD PNe with both crystalline and amorphous silicates have larger surface brightness and smaller diameters than all the other MD and ORD PNe. We suggest that they had the most massive and metal-rich progenitors, and that they can evolve to form MD PNe with only crystalline silicates in their spectra. ORD PNe have in general slightly lower surface brightness and slightly larger diameters than MD PNe, maybe indicating that their progenitors were not as massive or metal rich. ORD PNe with both crystalline and amorphous silicates might also evolve and form ORD PNe with only crystalline silicates, but the differences in the distributions of nebular diameters and $H\alpha$ surface brightness are not statistically significant in this case.

ACKNOWLEDGEMENTS

We thank the anonymous referee for comments that helped to improve the paper. This work is based in part on observations made

with the *Spitzer Space Telescope*, which was operated by the Jet Propulsion Laboratory, California Institute of Technology under a contract with NASA. This research has made use of the NASA/IPAC Infrared Science Archive, which is funded by the National Aeronautics and Space Administration and operated by the California Institute of Technology. This work received partial support from Dirección General de Asuntos del Personal Académico-Programa de Apoyo a Proyectos de Investigación e Innovación Tecnológica (DGAPA-PAPIIT) project IN 111423. D.H.-J. acknowledges support from a Mexican CONAHCYT scholarship.

DATA AVAILABILITY

The data underlying this article will be shared on reasonable request to the corresponding author.

REFERENCES

- Allamandola L. J., Tielens A. G. G. M., Barker J. R., 1989, *ApJS*, **71**, 733
 Barlow M. J., 1983, in Aller L. H., ed., Vol. 103, Planetary Nebulae. pp 105–128
 Bernal J. J., Haenecour P., Howe J., Zega T. J., Amari S., Ziurys L. M., 2019, *ApJ*, **883**, L43
 Bernard-Salas J., Tielens A. G. G. M., 2005, *A&A*, **431**, 523
 Bernard Salas J., Pottasch S. R., Feibelman W. A., Wesselius P. R., 2002, *A&A*, **387**, 301
 Cami J., de Jong T., Justtannont K., Yamamura I., Waters L. B. F. M., 1998, *Ap&SS*, **255**, 339
 Cernicharo J., 2004, *ApJ*, **608**, L41
 Cox N. L. J., Pilleri P., Berné O., Cernicharo J., Joblin C., 2016, *MNRAS*, **456**, L89
 Delgado-Inglada G., Rodríguez M., Peimbert M., Stasińska G., Morisset C., 2015, *MNRAS*, **449**, 1797
 Emerson J. P., Habing H. J., Clegg P. E., Lundy S., 1985, The IRAS mission, In its Infrared Astron. Satellite (IRAS) Catalogs and Atlases 23 p (SEE N85-18898 09-89)
 Fasano G., Franceschini A., 1987, *MNRAS*, **225**, 155
 Frew D. J., Parker Q. A., Bojičić I. S., 2016, *MNRAS*, **455**, 1459

- García-Hernández D. A., Górný S. K., 2014, *A&A*, **567**, A12
- Goebel J. H., Moseley S. H., 1985, *ApJ*, **290**, L35
- Górný S. K., Stasińska G., Szczerba R., Tyłenda R., 2001, *A&A*, **377**, 1007
- Grishko V. I., Tereszchuk K., Duley W. W., Bernath P., 2001, *ApJ*, **558**, L129
- Gutenkunst S., Bernard-Salas J., Pottasch S. R., Sloan G. C., Houck J. R., 2008, *ApJ*, **680**, 1206
- Guzman-Ramirez L., Zijlstra A. A., Níchuimín R., Gesicki K., Lagadec E., Millar T. J., Woods P. M., 2011, *MNRAS*, **414**, 1667
- Guzmán-Ramírez L., Zijlstra A., Níchuimín R., Gesicki K., Lagadec E., Millar T. J., Woods P. M., 2012, in *Planetary Nebulae: An Eye to the Future*. pp 259–262, doi:10.1017/S1743921312011052
- Hasselquist S., et al., 2020, *ApJ*, **901**, 109
- Helou G., 1995, in Haas M. R., Davidson J. A., Erickson E. F., eds, *Astronomical Society of the Pacific Conference Series Vol. 73, From Gas to Stars to Dust*. p. 681
- Hernández-Juárez D., Rodríguez M., Peña M., 2024, *Rev. Mex. Astron. Astrofis.*, **60**, 227
- Higdon S. J. U., et al., 2004, *PASP*, **116**, 975
- Hony S., Waters L. B. F. M., Tielens A. G. G. M., 2001, *A&A*, **378**, L41
- Hony S., Waters L. B. F. M., Tielens A. G. G. M., 2002a, *A&A*, **390**, 533
- Hony S., Bouwman J., Keller L. P., Waters L. B. F. M., 2002b, *A&A*, **393**, L103
- Houck J. R., et al., 2004, *ApJS*, **154**, 18
- Iben Jr. I., Renzini A., eds, 1981, *Physical processes in red giants Astrophysics and Space Science Library Vol. 88*, doi:10.1007/978-94-009-8492-9.
- Jones O. C., et al., 2017, *MNRAS*, **470**, 3250
- Karakas A. I., 2014, *MNRAS*, **445**, 347
- Karakas A. I., Lugaro M., 2016, *ApJ*, **825**, 26
- Kemper F., Waters L. B. F. M., de Koter A., Tielens A. G. G. M., 2001, *A&A*, **369**, 132
- Kessler M. F., 2002, *Advances in Space Research*, **30**, 1957
- Lewis M. O., Pihlström Y. M., Sjouwerman L. O., Stroh M. C., Morris M. R., BAaDE Collaboration 2020, *ApJ*, **892**, 52
- Matsuura M., et al., 2004, *ApJ*, **604**, 791
- Molster F. J., et al., 1999, *Nature*, **401**, 563
- Molster F. J., Waters L. B. F. M., Tielens A. G. G. M., Barlow M. J., 2002, *A&A*, **382**, 184
- Nuth J. A., Moseley S. H., Silverberg R. F., Goebel J. H., Moore W. J., 1985, *ApJ*, **290**, L41
- Papoular R., 2011, *MNRAS*, **415**, 494
- Parker Q. A., Bojičić I. S., Frew D. J., 2016, in *Journal of Physics Conference Series*. IOP, p. 032008 (arXiv:1603.07042), doi:10.1088/1742-6596/728/3/032008
- Perea-Calderón J. V., García-Lario P., Szczerba R., Bobrowsky M., 2009, *A&A*, **495**, L5
- Persi P., Cesarsky D., Marenzi A. R., Preite-Martinez A., Rouan D., Siebenmorgen R., Lacombe F., Tiphene D., 1999, *A&A*, **351**, 201
- Pottasch S. R., et al., 1984, *ApJ*, **278**, L33
- Pottasch S. R., Preite-Martinez A., Olmon F. M., Mo J. E., Kingma S., 1986, *A&A*, **161**, 363
- Press William H V. W. T., Saul T., 2007, *Numerical recipes 3rd edition: The art of scientific computing*. Cambridge university press
- Quireza C., Rocha-Pinto H. J., Maciel W. J., 2007, *A&A*, **475**, 217
- Rees N. R., Izzard R. G., Karakas A. I., 2024, *MNRAS*, **527**, 9643
- Roche P. F., Aitken D. K., 1986, *MNRAS*, **221**, 63
- Roche P. F., Aitken D. K., Whitmore B., 1983, *MNRAS*, **204**, 1017
- Scalo J. M., Despain K. H., Ulrich R. K., 1975, *ApJ*, **196**, 805
- Schneider R., Maiolino R., 2024, *A&ARv*, **32**, 2
- Stanghellini L., García-Lario P., García-Hernández D. A., Perea-Calderón J. V., Davies J. E., Manchado A., Villaver E., Shaw R. A., 2007, *ApJ*, **671**, 1669
- Stanghellini L., García-Hernández D. A., García-Lario P., Davies J. E., Shaw R. A., Villaver E., Manchado A., Perea-Calderón J. V., 2012, *ApJ*, **753**, 172
- Stasińska G., Szczerba R., 1999, *A&A*, **352**, 297
- Sylvester R. J., Kemper F., Barlow M. J., de Jong T., Waters L. B. F. M., Tielens A. G. G. M., Omont A., 1999, *A&A*, **352**, 587
- Ventura P., Karakas A., Dell’Aglì F., García-Hernández D. A., Guzman-Ramirez L., 2018, *MNRAS*, **475**, 2282
- Waters L. B. F. M., et al., 1996, *A&A*, **315**, L361
- Waters L. B. F. M., et al., 1998, *A&A*, **331**, L61
- Weiss A., Ferguson J. W., 2009, *A&A*, **508**, 1343
- Werner M. W., et al., 2004, *ApJS*, **154**, 1
- Whittet D., 2002, *Dust in the Galactic Environment*. CRC Press
- Zhang C. Y., Kwok S., 1990, *A&A*, **237**, 479
- de Vries B. L., Blommaert J. A. D. L., Waters L. B. F. M., Waelkens C., Min M., Lombaert R., Van Winckel H., 2014, *A&A*, **561**, A75

APPENDIX A: SPECTRA NOT PREVIOUSLY PUBLISHED

In this appendix, we present PN spectra from the *Spitzer Space Telescope* that have not been previously published. We do not show the data for four PNe with very noisy spectra (labelled as "poor quality" in Table [B1](#)).

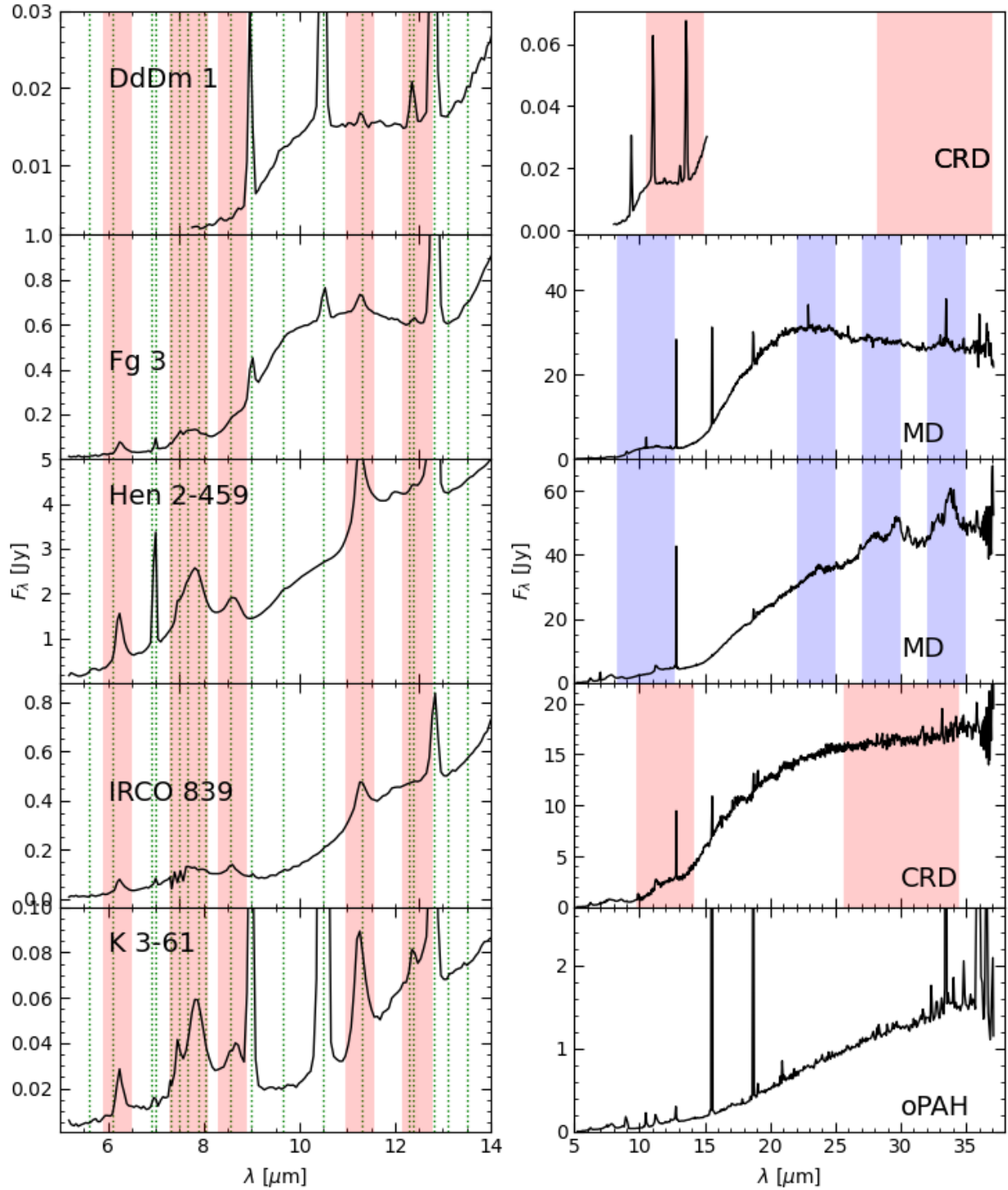


Figure A1. Previously unpublished PN spectra from the *Spitzer Space Telescope*. The left panels show the spectral region between 5 and 14 μm , with the pink bands marking the positions of the PAH features and the green dotted lines the wavelengths of nebular lines (listed in Fig. 1). The right panels show the region from 5 to 38 μm , with the pink bands around 12 and 30 μm indicating the positions of the SiC and 30 μm features, and the blue bands indicating the positions of the silicate features.

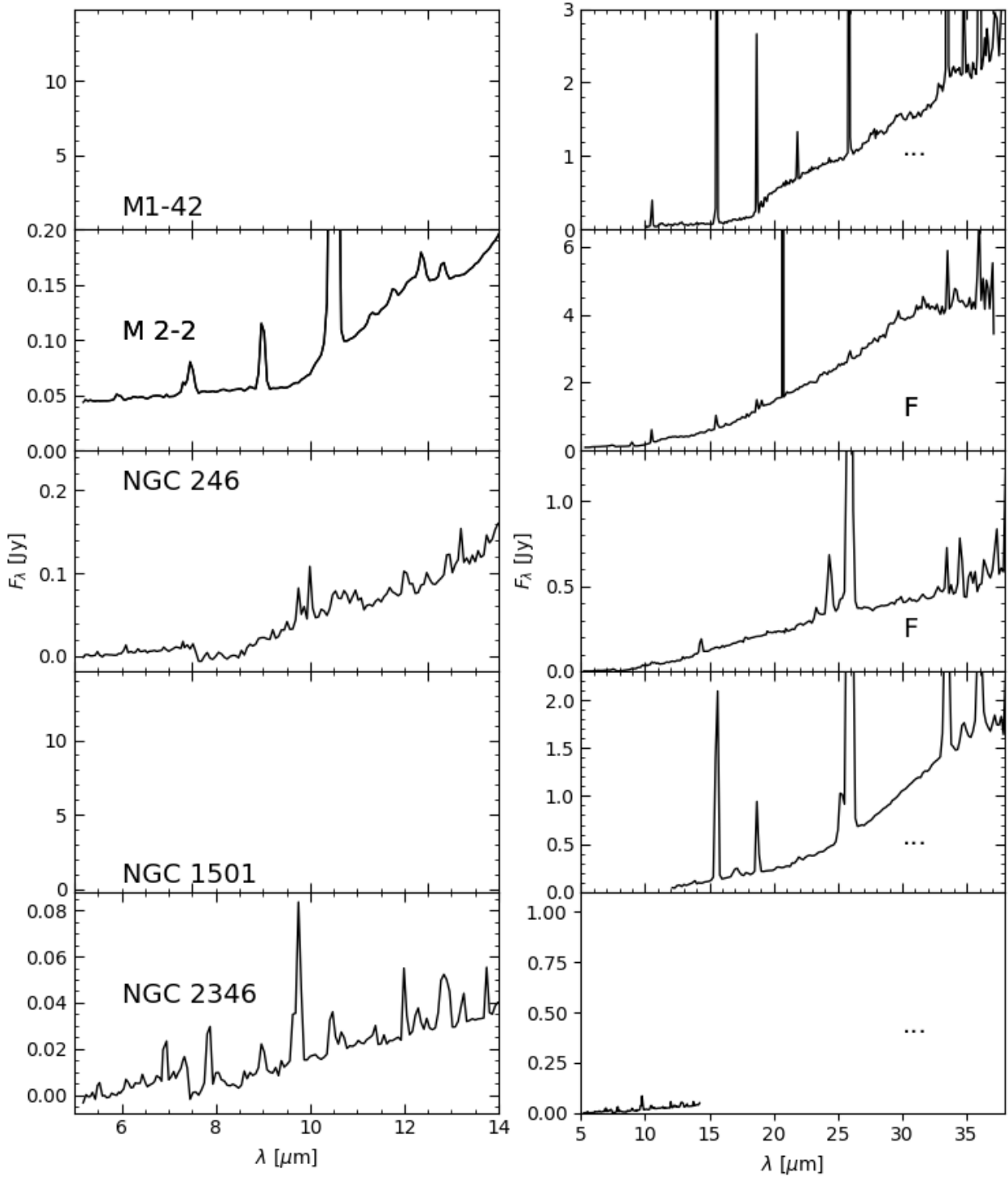


Figure A2. Previously unpublished PN spectra from the *Spitzer Space Telescope*. The left panels show the spectral region between 5 and 14 μm . The right panels show the region from 5 to 38 μm .

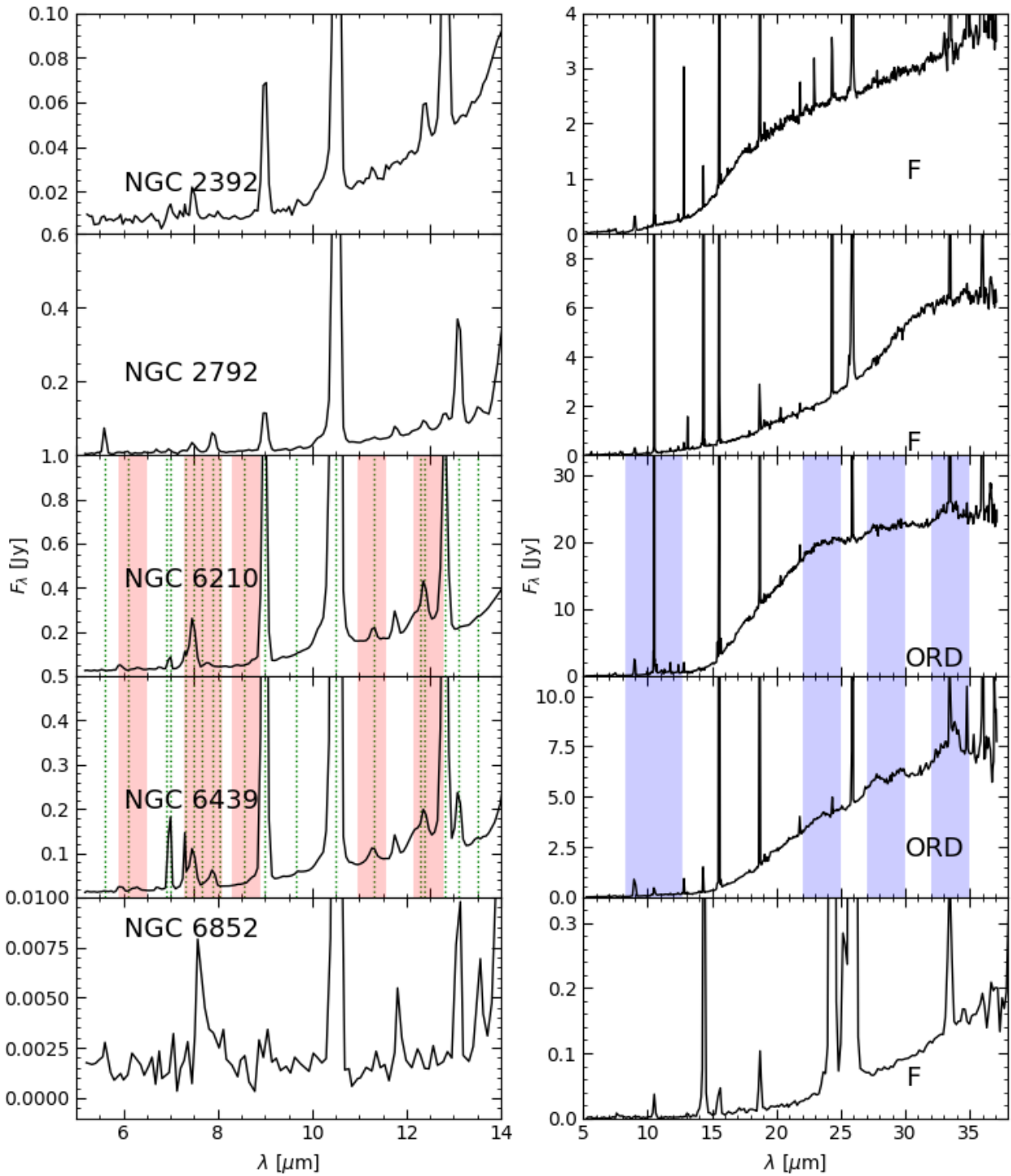


Figure A3. Previously unpublished PN spectra from the *Spitzer Space Telescope*. The left panels show the spectral region between 5 and 14 μm , with the pink bands marking the positions of the PAH features and the green dotted lines the wavelengths of nebular lines (listed in Fig. 1). The right panels show the region from 5 to 38 μm , where the blue bands indicate the positions of the silicate features.

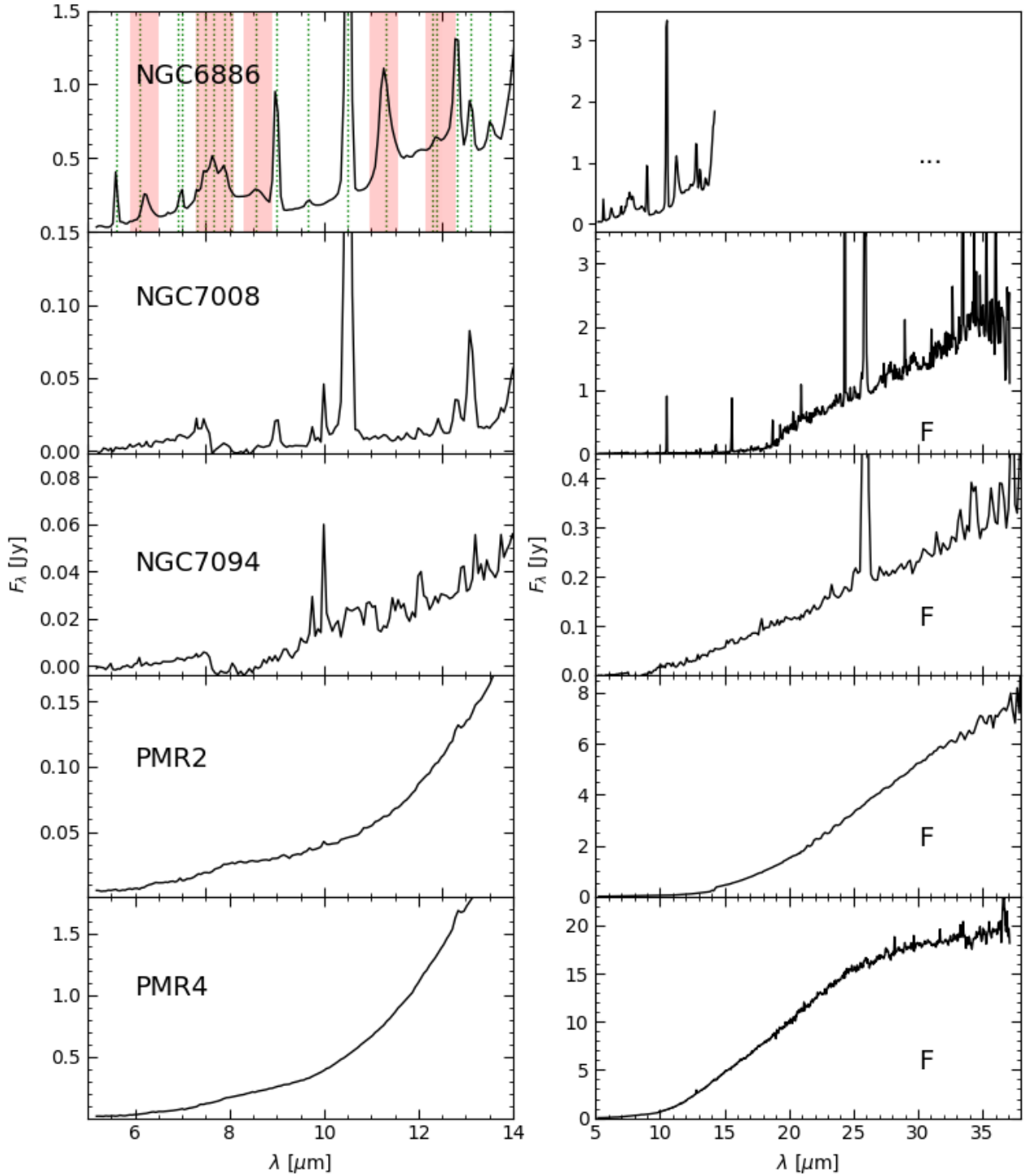


Figure A4. Previously unpublished PN spectra from the *Spitzer Space Telescope*. The left panels show the spectral region between 5 and 14 μm , with the pink bands marking the positions of the PAH features and the green dotted lines the wavelengths of nebular lines (listed in Fig. 1). The right panels show the region from 5 to 38 μm .

APPENDIX B: DUST TYPES

In this appendix, we present the identifications of the dust features for each PN and its classification according to these features. In the first and second columns of the table, we identify the PNe with their common name and PN G number. In the third column, we indicate the dust type (MD, ORD, CRD, PAH, or F) if it could be determined. In columns 4 to 8, the feature identifications of PAHs, SiC, 30 μm , and crystalline and amorphous silicates are indicated. The last two columns list the telescope and the reference for the published spectrum, respectively.

Table B1: Dust features and final classification of the PNe.

Name	PN G	Type	PAH	SiC	30 μm	Am. sil.	Crys. sil.	Origin	Ref.
19W32	359.2+01.2	...	×	×	...	✓	...	IRAS	R86
Abell 43	036.0+17.6	×	×	×	×	Spitzer	poor quality
A12-E	359.3+03.6	ORD	×	×	×	×	✓	Spitzer	S12
A12-F	358.5+02.9	F	×	×	×	×	×	Spitzer	S12
A12-R	358.7-02.7	ORD	×	×	×	✓	×	Spitzer	S12
B13-15	000.6-01.3	oPAH	✓	×	×	×	×	Spitzer	S12
B1B	358.3+01.2	MD	✓	×	×	×	✓	Spitzer	S12
B1Q	001.6-01.3	ORD	×	×	×	×	✓	Spitzer	G08
BoBn 1	108.4-76.1	oPAH	✓	×	×	×	×	Spitzer	S12
Cn 1-1	330.7+04.1	...	×	×	...	×	...	IRAS	P84
Cn 1-3	345.0-04.9	ORD	×	×	×	×	✓	Spitzer	PC09
Cn 1-5	002.2-09.4	MD	✓	×	×	×	✓	Spitzer	PC09
Cn 2-1	356.2-04.4	ORD	×	×	×	✓	✓	Spitzer	S12
CRL 618	166.4-06.5	...	×	×	...	×	...	IRAS	P86
CTS 1	019.8+05.6	F	×	×	×	×	×	Spitzer	S12
DdDm 1	061.9+41.3	CRD	...	✓	...	×	...	Spitzer	t.w.
Fg 3	352.9-07.5	MD	✓	×	×	✓	✓	Spitzer	t.w.
GJJC 1	009.8-07.5	F	×	×	×	×	×	Spitzer	S12
H 1-4	351.3+07.6	ORD	×	×	×	✓	×	Spitzer	S12
H 1-8	352.6+03.0	MD	✓	×	×	×	✓	Spitzer	S12
H 1-9	355.9+03.6	ORD	×	×	×	✓	×	Spitzer	S12
H 1-15	001.4+05.3	ORD	×	×	×	×	✓	Spitzer	G08
H 1-16	000.1+04.3	MD	✓	×	×	×	✓	Spitzer	PC09
H 1-17	358.3+01.2	MD	✓	✓	×	✓	✓	Spitzer	S12
H 1-18	357.6+02.6	MD	✓	×	×	×	✓	Spitzer	S12
H 1-19	358.9+03.4	MD	✓	×	×	×	✓	Spitzer	S12
H 1-20	358.9+03.2	MD	✓	×	×	×	✓	Spitzer	G08
H 1-21	348.4-04.1	MD	✓	×	×	×	✓	Spitzer	S12
H 1-22	350.8-02.4	ORD	×	×	×	×	✓	Spitzer	S12
H 1-23	357.6+01.7	ORD	×	×	×	✓	✓	Spitzer	S12
H 1-29	355.2-02.5	MD	✓	×	×	×	✓	Spitzer	S12
H 1-32	355.6-02.7	ORD	×	×	×	✓	✓	Spitzer	PC09
H 1-33	355.7-03.0	MD	✓	×	×	×	✓	Spitzer	S12
H 1-34	005.5+02.7	MD	✓	×	×	×	✓	Spitzer	S12
H 1-35	355.7-03.5	ORD	×	×	×	✓	×	Spitzer	PC09
H 1-40	359.7-02.6	MD	✓	×	×	✓	✓	Spitzer	PC09
H 1-43	357.1-04.7	MD	✓	×	×	×	✓	Spitzer	PC09
H 1-44	358.9-03.7	MD	✓	×	×	×	✓	Spitzer	S12
H 1-46	358.5-04.2	ORD	×	×	×	✓	✓	Spitzer	S12
H 1-53	004.3-02.6	MD	✓	×	×	×	✓	Spitzer	S12
H 1-56	001.7-04.6	ORD	×	×	×	×	✓	Spitzer	S12
H 1-61	006.5-03.1	MD	✓	×	×	×	✓	Spitzer	PC09
H 2-11	000.7+04.7	MD	✓	×	×	×	✓	Spitzer	G08
H 2-13	357.2+02.0	MD	✓	×	×	×	✓	Spitzer	S12
H 2-17	003.1+03.4	MD	✓	×	×	×	✓	Spitzer	S12
H 2-27	356.5-03.6	ORD	×	×	×	×	✓	Spitzer	S12
H 2-31	001.7-01.6	ORD	×	×	✓	×	×	Spitzer	S12
H 2-32	000.6-02.3	MD	✓	×	×	✓	✓	Spitzer	S12
H 2-39	002.9-03.9	F	×	×	×	×	×	Spitzer	S12
H 2-46	000.8-07.6	oPAH	✓	×	×	×	×	Spitzer	S12
H 2-48	011.3-09.4	ORD	×	×	×	✓	×	Spitzer	S12

Table B1 (continued): Dust features and final classification of the PNe.

Name	PN G	Type	PAH	SiC	30 μ m	Am. sil.	Crys. sil.	Origin	Ref.
Hb 4	003.1+02.9	ORD	×	×	×	×	✓	Spitzer	PC09
Hb 5	359.3–00.9	CRD	...	✓	✓	×	×	ISO	H02a
Hb 6	007.2+01.8	ORD	×	×	×	×	✓	Spitzer	PC09
Hb 7	003.9–14.9	ORD	×	×	×	✓	×	Spitzer	S12
Hb 12	111.8–02.8	...	×	×	...	✓	...	IRAS	P86
Hen 2–5	264.4–12.7	CRD	×	×	✓	×	×	Spitzer	S12
Hen 2–21	275.3–04.7	CRD	×	×	✓	×	×	Spitzer	S12
Hen 2–62	295.3–09.3	ORD	×	×	×	✓	×	Spitzer	S12
Hen 2–63	289.8+07.7	oPAH	✓	×	×	×	×	Spitzer	S12
Hen 2–68	294.9–04.3	CRD	✓	✓	✓	×	×	Spitzer	S12
Hen 2–73	296.3–03.0	MD	✓	×	×	✓	✓	Spitzer	S12
Hen 2–78	297.4+03.7	oPAH	✓	×	×	×	×	Spitzer	S12
Hen 2–86	300.7–02.0	MD	✓	×	×	✓	✓	Spitzer	S12
Hen 2–95	307.5–04.9	MD	✓	×	×	✓	✓	Spitzer	S12
Hen 2–99	309.0–04.2	oPAH	✓	×	×	×	×	Spitzer	S12
Hen 2–108	316.1+08.4	ORD	×	×	×	✓	✓	Spitzer	S12
Hen 2–113	321.0+03.9	MD?	✓?	×	×	✓	✓	ISO/IRAS	W98, M99
Hen 2–115	321.3+02.8	CRD	×	✓	✓	×	×	Spitzer	S12
Hen 2–125	324.2+02.5	MD	✓	×	×	×	✓	Spitzer	S12
Hen 2–129	325.0+03.2	ORD	×	×	×	×	✓	Spitzer	S12
Hen 2–133	324.8–01.1	MD	✓	×	×	✓	✓	Spitzer	S12
Hen 2–140	327.1–01.8	MD	✓	×	×	×	✓	Spitzer	S12
Hen 2–149	329.4–02.7	F	×	×	×	×	×	Spitzer	S12
Hen 2–151	326.0–06.5	ORD	×	×	×	✓	✓	Spitzer	S12
Hen 2–157	331.0–02.7	ORD	×	×	×	✓	✓	Spitzer	S12
Hen 2–178	344.2+04.7	ORD?	✓?	×	×	✓	×	Spitzer	S12
Hen 2–186	336.3–05.6	MD	✓	×	×	×	✓	Spitzer	S12
Hen 2–248	341.5–09.1	F	×	×	×	×	×	Spitzer	S12
Hen 2–26	278.6–06.7	CRD	✓?	✓	✓	×	×	Spitzer	S12
Hen 2–260	008.2+06.8	ORD	×	×	×	✓	×	Spitzer	PC09
Hen 2–262	001.2+02.1	ORD	×	×	×	×	✓	Spitzer	G08
Hen 2–306	348.8–09.0	F	×	×	×	×	×	Spitzer	S12
Hen 2–406	008.6–07.0	F	×	×	×	×	×	Spitzer	S12
Hen 2–438	064.7+05.0	MD	✓	×	×	✓	✓	ISO	BS05
Hen 2–440	060.5+01.8	MD	✓	×	×	✓	✓	Spitzer	S12
Hen 2–459	068.3–02.7	MD	✓	×	×	×	✓	Spitzer	t.w.
Hen 3–1132	336.9+08.3	ORD?	×	×	×	✓?	×	Spitzer	S12
Hen 3–1333	332.9–09.9	...	×	×	...	×	...	IRAS	P86
Hen 3–1716	014.0–05.5	F	×	×	×	×	×	Spitzer	S12
Hu 2–1	051.4+09.6	CRD	×	✓	...	×	...	IRAS	R86
IC 418	215.2–24.2	CRD	×	✓	×	×	×	Spitzer/ISO	H02a
IC 2003	161.2–14.8	MD	✓	×	×	×	✓	Spitzer	S12
IC 4732	010.7–06.4	MD	✓?	×	×	✓	✓	Spitzer	PC09
IC 4776	002.0–13.4	MD	✓	×	×	✓	✓	Spitzer	PC09
IC 4846	027.6–09.6	ORD	×	×	×	✓?	×	Spitzer	S12
IC 4997	058.3–10.9	...	×	×	...	×	...	IRAS	B83
IC 5117	089.8–05.1	×	...	×	...	IRAS	Z90
IRCO 839	110.1+01.9	CRD	✓	✓	×	×	×	Spitzer	t.w.
K 2–16	352.9+11.4	×	✓	×	×	ISO	H02a
K 3–6	031.0+04.1	MD	✓	×	×	✓	✓	Spitzer	S12
K 3–11	023.8–01.7	MD	✓	×	×	×	✓	Spitzer	S12
K 3–13	034.0+02.2	ORD	×	×	×	×	✓	Spitzer	S12
K 3–14	042.0+05.4	ORD	×	×	×	✓	×	Spitzer	S12
K 3–15	041.8+04.4	CRD	✓	✓	×	×	×	Spitzer	S12
K 3–17	039.8+02.1	MD	✓	×	×	×	✓	Spitzer/ISO	S12
K 3–19	032.9–02.8	CRD	✓	✓	✓	×	×	Spitzer	S12
K 3–20	032.5–03.2	MD	✓	×	×	×	✓	Spitzer	S12
K 3–29	048.1+01.1	CRD	✓	×	✓	×	×	Spitzer	S12

Table B1 (continued): Dust features and final classification of the PNe.

Name	PN G	Type	PAH	SiC	30 μ m	Am. sil.	Crys. sil.	Origin	Ref.
K 3–31	052.9+02.7	CRD	✓	✓	✓	×	×	Spitzer	S12
K 3–33	045.9–01.9	MD	✓	×	×	×	✓	Spitzer	S12
K 3–37	059.4+02.3	CRD	×	✓	✓	×	×	Spitzer	S12
K 3–39	059.9+02.0	CRD	✓	✓	✓	×	×	Spitzer	S12
K 3–40	058.9+01.3	ORD	×	×	×	×	✓	Spitzer	S12
K 3–43	055.1–01.8	F	×	×	×	×	×	Spitzer	S12
K 3–49	069.2+02.8	ORD	×	×	×	✓	✓	Spitzer	S12
K 3–52	067.9–00.2	MD	✓	×	×	×	✓	Spitzer	S12
K 3–54	063.8–03.3	CRD	✓?	✓	✓	×	×	Spitzer	S12
K 3–56	079.9+06.4	CRD	×	×	✓	×	×	Spitzer	S12
K 3–60	098.2+04.9	CRD	✓	✓	✓	×	×	Spitzer	S12
K 3–61	096.3+02.3	oPAH	✓	×	×	×	×	Spitzer	t.w.
K 3–62	095.2+00.7	CRD	✓	✓	✓	×	×	Spitzer	S12
K 3–78	088.7+04.6	F	×	×	×	×	×	Spitzer	S12
K 3–87	107.4–02.6	CRD?	×	×	✓?	×	×	Spitzer	S12
K 4–8	025.3–04.6	F	×	×	×	×	×	Spitzer	S12
K 4–16	048.5+04.2	CRD?	×	×	✓?	×	×	Spitzer	S12
K 4–19	038.4–03.3	F	×	×	×	×	×	Spitzer	S12
K 4–41	068.7+01.9	ORD	×	×	×	×	✓	Spitzer	S12
K 5–4	351.9–01.9	MD	✓	×	×	✓	✓	Spitzer	S12
KFL 4	003.0–02.6	CRD	×	×	✓	×	×	Spitzer	S12
KFL 12	003.2–04.4	F	×	×	×	×	×	Spitzer	S12
KW97 58–15	093.9–00.1	oPAH	✓	×	×	×	×	ISO/IRAS	P86, W98
M 1–5	184.0–02.1	CRD	✓	✓	✓	×	×	Spitzer	S12
M 1–6	211.2–03.5	...	×	×	...	✓	...	IRAS	R86
M 1–11	232.8–04.7	×	IRAS	Z90
M 1–12	235.3–03.9	CRD	×	✓	×	×	×	Spitzer	S12
M 1–20	006.1+08.3	CRD	✓	✓	✓	×	×	Spitzer	PC09
M 1–25	004.9+04.9	MD	✓	×	×	×	✓	Spitzer	PC09
M 1–26	358.9–00.7	...	×	✓?	...	×	...	IRAS	Z90
M 1–27	356.5–02.3	MD	✓	×	×	×	✓	Spitzer	PC09
M 1–31	006.4+02.0	MD	✓	×	×	×	✓	Spitzer	PC09
M 1–32	011.9+04.2	...	×	Spitzer	PC09
M 1–33	013.1+04.1	ORD	×	×	×	✓?	✓	Spitzer	PC09
M 1–35	107.4–06.6	×	×	×	✓	Spitzer	S12
M 1–37	002.6–03.4	MD	✓	×	×	×	✓	Spitzer	S12
M 1–38	002.4–03.7	MD	✓	×	×	×	✓	Spitzer	S12
M 1–40	008.3–01.1	MD	✓	×	×	×	✓	Spitzer	PC09
M 1–42	002.7–04.8	×	×	×	×	Spitzer	t.w.
M 1–45	012.6–02.7	MD	✓	×	×	×	✓	Spitzer	S12
M 1–51	020.9–01.1	MD	✓	×	×	×	✓	Spitzer	PC09
M 1–60	019.7–04.5	MD	✓	×	×	×	✓	Spitzer	PC09
M 1–61	019.4–05.3	MD	✓	×	×	✓	✓	Spitzer	S12
M 1–62	012.5–09.8	F?	×	×	×	×	×	Spitzer	S12
M 1–65	043.1+03.8	F	×	×	×	×	×	Spitzer	S12
M 1–69	038.7–03.3	ORD	×	×	×	×	✓	Spitzer	S12
M 1–71	055.5–00.5	CRD	✓	✓	✓	×	×	Spitzer	S12
M 2–2	147.8+04.1	F	×	×	×	×	×	Spitzer	t.w.
M 2–5	351.2+05.2	MD	✓	×	×	×	✓	Spitzer	G08
M 2–10	358.3+01.2	MD	✓	×	×	×	✓	Spitzer	S12
M 2–14	004.1–03.8	ORD	×	×	×	×	✓	Spitzer	S12
M 2–20	000.4–01.9	×	×	×	×	Spitzer	poor quality
M 2–23	002.2–02.7	ORD	×	×	×	✓	×	Spitzer	S12
M 2–27	359.9–04.5	MD	✓	×	×	×	✓	Spitzer	PC09
M 2–31	006.0–03.6	MD	✓	×	×	×	✓	Spitzer	S12
M 2–39	008.1–04.7	ORD	×	×	×	✓	✓	Spitzer	S12
M 2–42	008.2–04.8	F	×	×	×	×	×	Spitzer	S12
M 2–43	027.6+04.2	✓?	...	×	...	IRAS	Z90

Table B1 (continued): Dust features and final classification of the PNe.

Name	PN G	Type	PAH	SiC	30 μ m	Am. sil.	Crys. sil.	Origin	Ref.
M2-50	097.6-02.4	ORD?	×	×	×	✓?	×	Spitzer	S12
M2-51	103.2+00.6	...	×	×	×	×	✓	Spitzer	poor quality
M3-8	051.0+02.8	ORD	×	×	×	✓	✓	Spitzer	S12
M3-10	358.2+03.6	ORD	×	×	×	✓	✓	Spitzer	S12
M3-13	005.2+04.2	MD	✓	×	×	✓?	✓	Spitzer	PC09
M3-15	006.8+04.1	MD	✓	×	×	×	✓	Spitzer	PC09
M3-23	052.9-02.7	F	×	×	×	×	×	Spitzer	S12
M3-25	019.7+03.2	MD	✓	×	×	✓	✓	Spitzer	S12
M3-27	043.3+11.6	MD	✓	×	×	✓	✓	Spitzer	S12
M3-35	071.6-02.3	...	×	×	...	✓	...	IRAS	Z90
M3-38	356.9+04.4	MD	✓	×	×	✓	✓	Spitzer	PC09
M3-39	004.0-11.1	...	✓	Spitzer	poor quality
M3-40	358.7+05.2	MD	✓	×	×	×	✓	Spitzer	S12
M3-44	359.3-01.8	MD	✓	×	×	×	✓	Spitzer	PC09
M3-47	000.3-02.8	F	×	×	×	×	×	Spitzer	S12
M3-50	357.1-06.1	F	×	×	×	×	×	Spitzer	S12
M3-54	018.6-02.2	F	×	×	×	×	×	Spitzer	S12
M4-5	000.7+03.2	ORD	×	×	×	×	✓	Spitzer	G08
M4-6	358.6+01.8	MD?	✓?	×	×	×	✓	Spitzer	S12
M4-10	019.2-02.2	ORD	×	×	×	✓	✓	Spitzer	S12
M4-18	013.4-03.9	CRD	✓	✓	×	×	×	Spitzer	S12
M57	063.1+13.9	×	...	×	...	ISO	P99
MA 13	023.9+01.2	MD	✓	×	×	✓	✓	Spitzer	S12
MaC 1-2	107.4-00.6	...	✓	Spitzer	S12
MaC 1-11	008.6-02.6	ORD?	×	×	×	×	✓?	Spitzer	S12
MaC 2-1	205.8-26.7	CRD	×	✓	✓	×	×	Spitzer	S12
MR 22	284.1-00.7	×	...	✓	ISO	M02
Mz 3	331.7-01.0	×	×	✓	✓	ISO	BS05
NGC 40	120.0+09.8	CRD	✓	✓	✓	×	×	Spitzer/ISO	H01
NGC 246	118.8-74.7	F	×	×	×	×	×	Spitzer	t.w.
NGC 650	311.1+03.4	F?	×	×	×	×	×	Spitzer	S12
NGC 1501	144.1+06.1	×	×	×	×	Spitzer	t.w.
NGC 1535	206.4-40.5	CRD?	×	×	✓?	×	×	Spitzer	S12
NGC 2346	215.6+03.6	...	✓	Spitzer	t.w.
NGC 2392	197.8+17.3	F	×	×	×	×	×	Spitzer	t.w.
NGC 2440	234.8+02.4	oPAH	✓	×	×	×	×	ISO	BS02
NGC 2792	265.7+04.1	F	×	×	×	×	×	Spitzer	t.w.
NGC 2867	278.1-05.9	MD	✓	×	×	×	✓	Spitzer	PC09
NGC 3132	272.1+12.3	ORD	×	×	×	×	✓	Spitzer	PC09
NGC 3242	261.0+32.0	...	×	×	...	×	...	IRAS	R83
NGC 3918	294.6+04.7	×	...	×	...	Spitzer	G08
NGC 5315	309.1-04.3	...	×	×	...	×	...	IRAS	P86
NGC 5882	327.8+10.0	...	×	×	...	×	...	IRAS	P86
NGC 6072	343.4+11.9	F	×	×	×	×	×	Spitzer	S12
NGC 6153	341.8+05.4	×	...	×	✓	ISO/IRAS	P86, BS05
NGC 6210	043.1+37.7	ORD	×	×	...	×	✓	Spitzer	t.w.
NGC 6302	349.5+01.0	MD	✓	×	×	✓?	✓	ISO	M02, BS05
NGC 6309	009.6+14.8	...	×	×	...	×	...	IRAS	R83
NGC 6369	002.4+05.8	CRD	×	×	✓	×	×	ISO	H01, H02b
NGC 6439	011.0+05.8	ORD	×	×	×	×	✓	Spitzer	t.w.
NGC 6537	010.0+00.7	×	×	×	✓	ISO/IRAS	P86, M02
NGC 6543	096.4+29.9	×	×	×	×	ISO/IRAS	P99, BS05
NGC 6567	011.7-06.6	CRD?	✓?	✓?	✓?	×	×	Spitzer	S12
NGC 6572	034.6+11.8	...	×	×	...	✓	...	IRAS	P86
NGC 6644	008.3-07.3	CRD	✓	✓	✓	×	×	Spitzer	PC09
NGC 6741	033.8-02.6	×	...	×	...	IRAS	R86
NGC 6790	037.8-06.3	...	×	×	...	×	...	IRAS	P86
NGC 6807	042.9-06.9	ORD	×	×	×	✓	✓	Spitzer	S12

Table B1 (continued): Dust features and final classification of the PNe.

Name	PN G	Type	PAH	SiC	30 μ m	Am. sil.	Crys. sil.	Origin	Ref.
NGC 6826	083.5–12.7	CRD	...	×	✓	×	×	ISO	H02a
NGC 6852	042.5–14.5	F	×	×	×	×	×	Spitzer	t.w.
NGC 6881	074.5+02.1	oPAH	✓	×	×	×	×	Spitzer	PC09
NGC 6884	082.1+07.0	...	×	×	...	×	...	IRAS	R86
NGC 6886	060.1–07.7	...	×	Spitzer	t.w.
NGC 7008	093.4+05.4	F	×	×	×	×	×	Spitzer	t.w.
NGC 7009	037.7–34.5	...	×	×	...	×	...	IRAS	P86
NGC 7026	089.0+00.3	...	×	×	...	×	...	IRAS	P86
NGC 7027	084.9–03.4	CRD	✓	✓	✓	×	×	ISO	H01, BS05
NGC 7094	066.7–28.2	F	×	×	×	×	×	Spitzer	t.w.
NGC 7354	107.8+02.3	...	×	×	...	×	...	IRAS	P86
NGC 7662	106.5–17.6	...	×	×	...	×	...	IRAS	P86
PB 2	263.0–05.5	CRD	×	✓	✓	×	×	Spitzer	S12
PBOZ 24	002.1+03.3	ORD	×	×	×	×	✓	Spitzer	G08
PBOZ 26	285.4+02.2	F	×	×	×	×	×	Spitzer	S12
Pe 1–1	285.4+01.5	CRD	✓	×	✓	×	×	Spitzer	S12
Pe 2–8	322.4–00.1	...	×	×	...	✓	...	IRAS	P86
Pe 2–10	006.8+02.0	ORD	×	×	×	×	✓	Spitzer	S12
Pe 2–15	026.0–01.8	F	×	×	×	×	×	Spitzer	S12
PMR 1	272.8+01.0	×	×	×	×	Spitzer	PC09
PMR 2	291.3+08.4	F	×	×	×	×	×	Spitzer	t.w.
PMR 4	014.2+03.8	F	×	×	×	×	×	Spitzer	t.w.
Sa 1–5	340.9–04.6	F	×	×	×	×	×	Spitzer	S12
Sa 2–6	258.0–15.7	×	×	×	✓	Spitzer	S12
Sa 2–157	325.8–12.8	ORD	×	×	×	✓	×	Spitzer	S12
Sa 2–208	344.4–06.1	F	×	×	×	×	×	Spitzer	S12
Sa 3–90	000.8–01.5	MD	✓	×	×	×	✓	Spitzer	S12
Sa 3–134	016.9–02.0	MD	✓	×	×	×	✓	Spitzer	S12
Sp 4–1	068.7+14.8	oPAH	✓	×	×	×	×	Spitzer	S12
SwSt 1	001.5–06.7	...	×	×	...	✓	...	IRAS	Z90
Th 3–6	354.9+03.5	MD	✓	×	×	×	✓	Spitzer	S12
Th 3–10	355.9+02.7	MD	✓	×	×	×	✓	Spitzer	S12
Th 3–12	356.8+03.3	MD	✓	×	×	×	✓	Spitzer	S12
Th 3–24	357.1+01.9	F	×	×	×	×	×	Spitzer	S12
Th 3–55	356.5+01.5	ORD	×	×	×	×	✓	Spitzer	S12
Th 4–3	006.0+02.8	MD	✓	×	×	✓	✓	Spitzer	S12
Th 4–6	009.3+04.1	ORD	×	×	×	✓	✓	Spitzer	S12
Vd 1–2	345.0+04.3	ORD	×	×	×	✓	×	Spitzer	S12
Vd 1–3	344.8+03.4	oPAH	✓	×	×	×	×	Spitzer	S12
Vd 1–5	344.4+02.8	oPAH?	✓?	×	×	×	×	Spitzer	S12
VV 3	014.3–05.5	CRD	✓	✓	✓	×	×	Spitzer	S12
Vy 2–2	045.4–02.7	×	...	✓	...	ISO	P99, H02a

References for the published spectra: B83: Barlow (1983), BS02: Bernard Salas et al. (2002), BS05: Bernard-Salas & Tielens (2005), G08: Gutenkunst et al. (2008), H01: Hony et al. (2001), H02a: Hony et al. (2002a), H02b: Hony et al. (2002b), M02: Molster et al. (2002), P84 Pottasch et al. (1984), P86: Pottasch et al. (1986), P99: Persi et al. (1999), PC09: Perea-Calderón et al. (2009), R83: Roche et al. (1983), R86: Roche & Aitken (1986), S12: Stanghellini et al. (2012), t.w.: this work, W98: Waters et al. (1998), Z90: Zhang & Kwok (1990).

Table C1. Objects where our classification differs from those of [Stanghellini et al. \(2012, S12\)](#) or [García-Hernández & Górný \(2014, GH14\)](#).

Name	PNG	S12	GH14	This work	Feature
A12-E	359.3+03.6	F	F	ORD	Crystalline silicates
H 1-33	355.7−03.0	oPAH	oPAH	MD	Crystalline silicates
H 2-27	356.5−03.6	F	...	ORD	Crystalline silicates
H 2-39	002.9−03.9	ORD	ORD	F	Crystalline silicates
Hen 2-63	289.8+07.7	F	F	oPAH	PAHs
Hen 2-186	336.3−05.6	oPAH	oPAH	MD	Crystalline silicates
Hen 2-440	060.5+01.8	ORD	ORD	MD	PAHs
IC 4776	002.0−13.4	MD	MD	ORD	PAHs
K 3-15	041.8+04.4	CRD	oPAH	CRD	SiC
K 3-29	048.1+01.1	oPAH	...	CRD	30 μm
K 4-8	025.3−04.6	ORD	ORD	F	Crystalline silicates
M 1-69	038.7−03.3	F	F	ORD	Crystalline silicates
M 2-10	354.2+04.3	oPAH	MD	MD	Crystalline silicates
M 2-14	003.6+03.1	...	MD	ORD	PAHs
M 3-8	358.2+04.2	...	MD	ORD	PAHs
NGC 6072	343.4+11.9	...	F	ORD	Crystalline silicates
Pe 1-1	285.4+01.5	oPAH	oPAH	CRD	30 μm
Th 4−6	009.3+04.1	ORD	MD	ORD	PAHs
VV 3	014.3−05.5	oPAH	oPAH	CRD	SiC

APPENDIX C: OBJECTS WITH DIFFERENT ASSIGNED TYPE

We present in Table C1 the list of objects in which our classification differs from those of [Stanghellini et al. \(2012\)](#) and [García-Hernández & Górný \(2014\)](#). We have used the features that these authors identify to translate their classification into our classification scheme. The differences are related to the presence or absence of the dust features listed in the last column of Table C1.

This paper has been typeset from a $\text{\TeX}/\text{\LaTeX}$ file prepared by the author.